Open-Phase-Tolerant Online Current References for Maximum Torque Range and Minimum Loss With Current and Torque-Ripple Limits for *n*-Phase Nonsalient PMSMs With Nonsinusoidal Back EMF

Alejandro G. Yepes[®], *Senior Member, IEEE*, Wessam E. Abdel-Azim[®], Abdullah Shawier[®], Ayman Samy Abdel-Khalik[®], *Senior Member, IEEE*, Mostafa S. Hamad, *Senior Member, IEEE*, Shehab Ahmed[®], *Senior Member, IEEE*, and Jesús Doval-Gandoy[®], *Member, IEEE*

Abstract -- Multiphase permanent-magnet synchronous machines (PMSMs) with nonsinusoidal back-electromotive force (back EMF) offer high fault tolerance and torque density for electric vehicles. Most current-reference generation methods either minimize stator copper loss (SCL) or maximize achievable torque. Optimization of both goals is accomplished by full-torque-range minimum-loss (FRML) strategies, but so far just for sinusoidal back EMF. Thus, FRML for nonsinusoidal back EMF should be sought. Moreover, many methods are only suitable for healthy conditions or specific machines, harmonics, or open-phase-fault (OPF) scenarios. In addition, the torque range may be extended by permitting torque ripple or (transiently) greater rms current, but this approach is not general nor FRML yet. This article proposes online FRML current-reference generation for multiphase PMSMs with nonsinusoidal back EMF: nonsinusoidal-back-EMF FRML (NSBE-FRML). When the torque reference is feasible, minimum SCL is attained while maximizing the achievable torque (i.e., FRML). For higher torque references, the instantaneous torque deviation is minimized, and the torque reference

Manuscript received 14 February 2023; revised 16 May 2023; accepted 19 June 2023. Date of publication 22 June 2023; date of current version 16 March 2024. This work was supported in part by the Information Technology Industry Development Agency (ITIDAs) Information Technology Academia Collaboration (ITAC) Funded Project within the category type of Advanced Research Projects (ARPs) under Grant ARP2020.R29.7; in part by the Government of Galicia under Grant ED431F 2020/07 and Grant GPC-ED431B 2020/03; in part by the Ministry of Science, Innovation and Universities under the Ramon y Cajal Grant RYC2018-024407-I; and in part by the Spanish State Research Agency (AEI) under Project PID2019-105612RB-100/AEI/10.13039/501100011033. (Corresponding author: Jesús Doval-Gandoy.)

Alejandro G. Yepes and Jesús Doval-Gandoy are with the Applied Power Electronics Technology (APET) Research Group, CINTECX, Universidade de Vigo, 36310 Vigo, Spain (e-mail: agyepes@uvigo.es; jdoval@uvigo.es).

Wessam E. Abdel-Azim, Abdullah Shawier, and Ayman Samy Abdel-Khalik are with the Electrical Engineering Department, Faculty of Engineering, Alexandria University, Alexandria 21544, Egypt (e-mail: wessam.essam@alexu.edu.eg; abdullah.shawier@alexu.edu.eg; ayman.abdel-khalik@alexu.edu.eg).

Mostafa S. Hamad is with the Research and Development Center, Arab Academy for Science, Technology and Maritime Transport, Al Alamein 51718, Egypt (e-mail: mostafa.hamad@staff.aast.edu).

Shehab Ahmed is with the CEMSE Division, King Abdullah University of Science and Technology, Thuwal 23955, Saudi Arabia (e-mail: shehab.ahmed@kaust.edu.sa).

This article has supplementary downloadable material available at https://doi.org/10.1109/TTE.2023.3288525, provided by the authors.

Digital Object Identifier 10.1109/TTE.2023.3288525

is saturated in consecutive samples limiting the torque ripple to a prespecified threshold. Furthermore, the rms current is limited after transient overload by automatically decreasing the torque reference. The NSBE-FRML is suitable for any harmonics, healthy/OPF conditions, and multiphase PMSMs with negligible saliency ratio. Experiments are performed with a six-phase PMSM

Index Terms—Fault tolerance, full-range minimum loss (ML), multiphase drives, nonsinusoidal back-electromotive force (back EMF), open-phase faults (OPFs), six-phase machine.

Nomenclature

Acronyms

Back EMF Back-electromotive force.
FRML Full-torque-range minimum loss.
IGBT Insulated-gate bipolar transistor.

ML Minimum loss.
MT Maximum torque.

MTPR Maximum torque per rms current.
MTPP Maximum torque per peak current.
NSBE-FRML Nonsinusoidal-back-EMF FRML.

OPF Open-phase fault.

PMSM Permanent-magnet synchronous machine.

SCL Stator copper loss.

Variables and Constants

 $\varepsilon_{\rm rms}$ Phase-current-rms excess from $i_{\rm rms}^{\rm mx}$.

e Column vector of phase back EMFs e_k .

f Column vector with 1 (healthy) or 0 (OPF) per phase.

 f_v Column vector with 1 for the phase currents that are variables for the SCL minimization (0 otherwise).

 f_{nv} Column vector with 1 for the phase currents that are not variables for the SCL minimization (0 otherwise).

 γ Integral of the phase-current-rms excess $\varepsilon_{\rm rms}$ from $i_{\rm rms}^{\rm mx}$.

i Column vector of phase currents i_k .

- i_{v} Vector i restrained as $i_{v} = f_{v} \circ i$.
- i_{nv} Vector i restrained as $i_{nv} = f_{nv} \circ i$.
- $i_{\rm nk}^{\rm mx}$ Maximum peak current (converter).
- $i_{\rm rms}^{\rm mx}$ Maximum steady-state rms current (machine).
- J SCL normalized by the stator resistance.
- *k* Stator phase (1 for phase a, 2 for phase b, and so on).
- $K_{\rm rms}$ Gain to set the dynamics of the rms-current limitation.
- κ_{+} Indices of healthy phases with e_k signs equal to σ_e .
- κ_{-} Indices of healthy phases with e_k signs not equal to σ_e .
- *n* Total number of phases.
- n_{κ}^{+} Number of κ_{+} elements.
- n_{κ}^{-} Number of κ_{-} elements.
- ρ Produces a rising edge if a transient overload finishes.
- σ_e Indicates if most e_k for healthy phases are positive (1), negative (-1), or neither is true (0).
- σ_t Indicates T sign: positive (1), negative (-1), or zero (0).
- τ_1 Fundamental period.
- T^{***} Input torque reference, set externally beforehand.
- T^{**} Variable used as an intermediate step of the rms-current limitation, holding the T^{***} value.
- T^* Reduced torque reference to limit the rms current.
- Reduced torque reference to limit the torque ripple. This value is used for the i reference generation.
- $T_{\rm d}$ Indicates if T is feasible (0) or not (1), respecting $i_{\rm pk}^{\rm mx}$. This implies $T_{\rm f}=T$ or $T_{\rm f}\neq T$, respectively.
- $T_{\rm exp}$ Experimental torque.
- $T_{\rm f}$ Final torque corresponding to the current references.
- T_{sat} Saturation limit T_{sat} applied to saturate T^* to T in order to limit the torque ripple to T_{th} .
- $T_{\rm th}$ Torque-ripple threshold for the torque-ripple limitation.
- T_1 Maximum T without reaching i_{pk}^{mx} in any phase.
- T_2 Maximum T without exceeding $i_{\text{rms}}^{\text{mx}}$ in any phase.
- T_3 Maximum T without T_f ripple.
- T_4 Maximum T with T_f ripple under T_{th} .

Other Symbols

- Elementwise product.
- |x| Elementwise absolute value of x.
- $\lfloor x \rfloor$ Floor function of x.
- x^{\perp} Nonconjugate transpose of x.

I. Introduction

ULTIPHASE electric machine drives offer several important advantages compared with three-phase ones [1], [2], [3]. The current ratings are lower for given power and voltage [3], [4], [5], [6], allowing lighter ac cables and alleviating the need of parallel converter switches [3]. Their suitability for integrated battery chargers with minimum reconfiguration makes them very convenient for electric

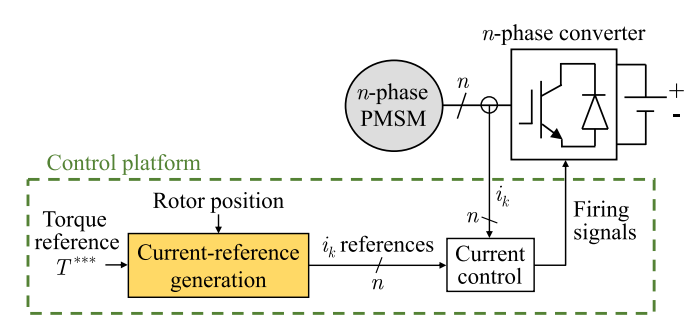


Fig. 1. Multiphase PMSM drive based on field-oriented control. This article is focused on the yellow-shaded block.

vehicles [7], [8]. Moreover, multiphase drives are able to continue operation under OPFs [1], [2], e.g., for limp-home mode in vehicles [9]. OPFs may be the result of open-circuit failures in the stator windings/connections or of isolating the phases affected by other types of faults (e.g., in the switches) [1], [2], [10], [11].

A key part of an ac machine drive based on field-oriented control is the generation of the current references for the inner current controller, so as to track an external torque reference (see Fig. 1). Multiple alternatives exist for this purpose in the literature, as summarized in Table I. For a multiphase machine without faults and without back-EMF harmonics, the current references are usually set balanced and sinusoidal. In case of OPFs, traditionally, the sinusoidal current references for these machines used to be set according to the so-called minimumloss (ML) or maximum torque (MT) strategies [1], [11], [12]. When using ML or MT, the current distribution among the phases is the same regardless of the torque; i.e., the sinusoidal phase-current waveforms are simply rescaled with the torque reference. For ML, the phase-current amplitudes are unequal, and the achievable torque is relatively low, because some of them reach the rated current soon, as the torque reference is raised. For MT, the current amplitudes are (normally) identical, allowing greater admissible torque, but at the expense of larger SCL per torque. More recently, the FRML strategy attained minimum SCL in the entire torque range, while maximizing the torque capability, by including the phase-current inequality constraints in the optimization problem [13]. Thus, the FRML method combines the strengths of ML and MT, without their weaknesses [13], [14], [15], as illustrated in Fig. 2, for an asymmetrical six-phase PMSM without saliency, with sinusoidal back EMF, and with one OPF [10], [13], [16]. As the torque increases beyond its maximum value for ML (e.g., 54% in Fig. 2), the FRML progressively raises some of the phase currents, so that the currents (and SCL) conveniently evolve from the ML ones to the MT ones. The FRML was enhanced for induction machines in [16] by allowing optimum current harmonics, so that higher torque could be obtained during transient overload, which is a very desirable feature in electric vehicles for overtaking, emergency braking, steep slopes, and so on [16], [17], [18]. Namely, the FRML current references were optimally generated in [16] while respecting the different current thresholds that are mainly associated with steady-state and transient conditions [17], [18]: the machine rms-current rating and the peak-current rating of the converter switches,

Method	References	1) Suitable for back-EMF harmonics	2) Mini- mum SCL per torque	1.1	n, healthy/OPFs,	need offline	· ·	7) Automatic transition from overload to steady state
ML	[1], [11]	×	✓	×	×	×	×	×
MT	[1], [11]	×	×	\checkmark	×	×	×	×
FRML*	[13]–[16]	×	\checkmark	\checkmark	×	×	×	×
MTPR	[18]–[26] [†]	\checkmark	\checkmark	×	\checkmark	\checkmark	×	×
MTPP	[17]–[20]	\checkmark	×	\checkmark	×	×	×	×
Torque-ripple allowance	[27]	\checkmark	×	×	×	×	\checkmark	×
Proposed NSBE-FRML	This paper	✓	\checkmark	✓	✓	✓	✓	\checkmark

TABLE I
SUMMARY OF THE FEATURES OF THE PROPOSED METHOD COMPARED WITH THE EXISTING LITERATURE

[†] If some of the methods within a group of references are more advantageous than others, the most positive features are considered.

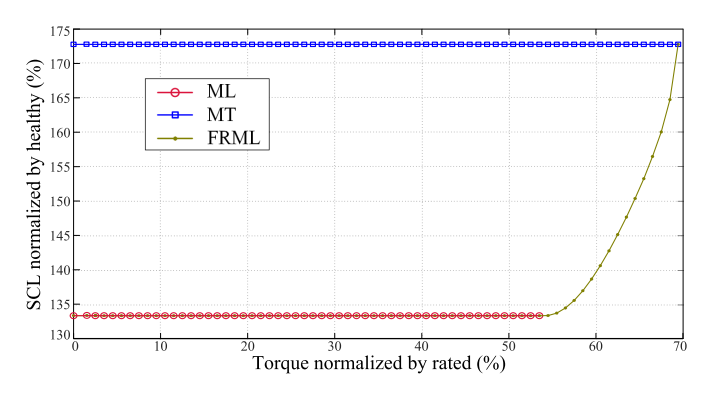


Fig. 2. Comparison of the ML, MT, and FRML strategies of sinusoidal current-reference generation for an asymmetrical six-phase PMSM without saliency and with sinusoidal back EMF, one stator neutral point, and one phase open [10], [13]. The torque is normalized by the rated torque, and the SCL is normalized by the SCL in healthy conditions for the same torque [16].

respectively. However, these FRML techniques [13], [14], [15], [16] are not suitable for PMSMs with nonsinusoidal back EMF, where they could cause considerable unnecessary torque oscillations. In brief, unlike ML and MT, FRML provides SCL-per-torque minimization and torque-range maximization at the same time, but so far only for machines without back-EMF harmonics.

Multiphase PMSMs with significant back-EMF harmonics are a popular choice [17], [18], [19], [20], [21], [22], [23], [24], [25], [26], [27], [28], [29], [30]. Principally, the nonsinusoidal back EMF makes it possible to yield higher torque density than sinusoidal back EMF [19], [20], [25]. The back-EMF harmonics can be achieved by an appropriate design of the stator windings and magnet magnetization, so that they give rise to notable winding-function and flux harmonics, respectively [20]. In particular, although nonsinusoidal back EMF may be obtained with other types of windings, it is especially easy to produce in PMSMs with concentrated windings (containing large winding-function harmonics). These windings also offer several attractive features when using fractional slot per-pole-per-phase number that make them powerful candidates for electric vehicles [31], [32], despite their typically low (negligible) saliency ratio [2], [33], [34]. They exhibit high slot fill factor and power density [32], [35], low manufacturing cost [28], [29], [35] and cogging torque [35], [36], short end windings [28], [31], [35], [37], better filtering of undesired current harmonics [8], enhanced isolation between windings and tolerance to short-circuit faults [2], [34], [37], and so on. However, to exploit the greater torque capability of PMSMs with nonsinusoidal back EMF (regardless of the winding type), adequate current harmonics need to be injected [20], [22], [25]. Under OPFs, the addition of current harmonics becomes even more important, because they can be used to compensate the torque ripple produced by the interaction between the postfault fundamental phase-current imbalance and the back-EMF harmonics [23], [26], [30]. Thus, the generation of nonsinusoidal current references is key for fault-tolerant PMSMs with nonsinusoidal back EMF.

Due to the redundant degrees of freedom of multiphase PMSMs, the nonsinusoidal current waveforms to deliver a torque reference without torque ripple are not unique, even in the absence of OPFs. As shown in Table I, most of the existing solutions of current references for nonsinusoidal back EMF may be classified into MTPR [18], [19], [20], [21], [22], [23], [24], [25], [26], sometimes called maximum torque per ampere, and MTPP [17], [18], [19], [20]. MTPR minimizes the SCL (rms current) per torque and MTPP maximizes the torque range, similar to the ML and MT methods for sinusoidal back EMF, respectively. As ML and MT, MTPR and MTPP are also based on rescaling the current waveforms with the required torque. MTPR may be used at steady state, at which the rms-current rating of the machine is the main limitation, whereas MTPP may be employed to achieve larger torque during transient overload, when the peak current is limited by the rating of the converter switches [17], [18]. However, none of the available strategies for nonsinusoidal back EMF minimize the SCL for each torque value in the range between the maximum torque of MTPR and that of MTPP. This characteristic would allow better efficiency (greater driving range) as well as longer overload without machine overheating. To accomplish this goal, an FRML technique for PMSMs with nonsinusoidal back EMF, combining the advantages of MTPR (minimum SCL) and MTPP (maximum torque) in this context, should be sought. This would be analogous to the aforementioned FRML strategies

^{*} Although the FRML from [14], [15] is general and online to a significant extent, it relies on the ML offline optimization for each machine.

(which combine the ML and MT benefits; see Fig. 2) for machines with sinusoidal back EMF [13], [14], [15], [16], but instead for PMSMs with back-EMF harmonics.

On the other hand, many of these existing methods for nonsinusoidal back EMF are only suitable for a reduced number of current harmonics and back-EMF harmonics [17], [18], [19], [20], [25], [26], [27], [28], [29], [30]. Furthermore, some of them can only be applied to healthy operation [5], [17], [18], [19], [20], [25], a few specific OPF scenarios [27], [28], [29] or certain machines (phase number n, symmetrical/asymmetrical windings, and so on) [5], [17], [18], [19], [20], [25], [27], [28], [29]. Several MTPR methods are general concerning these features [21], [23], [24], but none of the MTPP ones are. This lack of generality is often manifested in the fact that offline optimization for particular conditions is needed. In this regard, if an FRML approach is to be developed, it should preferably be designed, so that it attains online optimization for any *n*-phase PMSM, any degree of back-EMF distortion, either healthy or OPF operation, and any kind of OPFs.

In addition, when enhancing the torque capability is crucial, certain amount of torque ripple may be allowed for raising the maximum mean torque that can be attained while respecting the current constraints. Xiong et al. [27] proposed to gradually relieve the constraint of minimum torque ripple, as the torque reference is increased, in a five-phase PMSM with third back-EMF harmonic. Unfortunately, the SCL is never minimized (it is not FRML), the ripple-free torque range is not maximized, it is designed just for a specific PMSM, and the phase currents are limited at all times by the rms rating without permitting greater rms current (and, hence, higher mean torque with lower ripple) during transient overload. Therefore, this kind of strategy with progressive torque-ripple allowance [27] could be substantially improved by integrating it into a new FRML algorithm (i.e., ensuring minimum SCL and maximum torque) that would also be general and suitable for transient torque overload.

In summary, several conclusions may be highlighted about the literature on the subject, in agreement with Table I. Note that seven points, called 1)-7) and corresponding to different columns, are distinguished in this table. Most importantly, for PMSMs with 1) nonsinusoidal back EMF, there are no methods able to 2) minimize the SCL per torque in the 3) maximum torque range. That is, none of the existing methods is assigned a green check mark for 1)-3) simultaneously in Table I. In other words, FRML has not been fulfilled for nonsinusoidal back EMF. This is the most relevant gap that motivates this article. In addition, there are also other desirable properties that are absent in most of the previous techniques and are not straightforward to combine with the FRML characteristic, but which should also be sought: 4) generality; 5) no need for offline optimization; 6) possible allowance of torque ripple as the torque increases beyond the maximum ripplefree torque so as to achieve extended torque range during overload; and 7) automatic gradual transition from overload to steady state (where peak-current and rms-current limits prevail, respectively).

In view of these gaps, this article proposes an FRML current-reference generation method to address them,

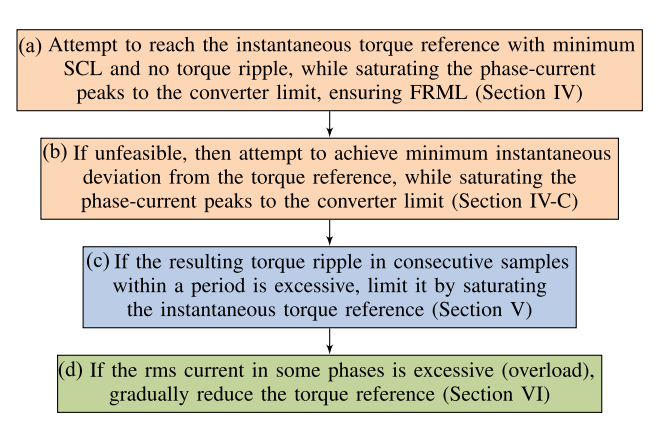


Fig. 3. Illustration of the general concept of the current-reference generation method proposed in this article (Sections III–VI).

as reflected in the last row of Table I. This new method may be called NSBE-FRML. The generated current references are suitable for n-phase PMSMs with nonsinusoidal back EMF and negligible saliency ratio, either in healthy or OPF conditions. The general concept is illustrated in Fig. 3, in which four stages a)-d) are defined. As long as it is possible, a) optimum current harmonics are injected to obtain the torque reference with minimum SCL and no torque ripple (smooth electromagnetic torque). Most importantly, this is achieved for higher torque values than in previous approaches aimed at minimum SCL, because the peak-current limitation is here taken into account as a constraint in the optimization, in FRML manner. That is, the SCL is minimized in the maximum possible range of ripple-free torque, as indicated in columns 2) and 3) of Table I. This is the first time that this FRML property is accomplished for nonsinusoidal back EMF. On the other hand, if the torque reference exceeds the ripple-free torque range and, hence, it cannot be reached at some instants of the fundamental period, b) the currents are set, so that the instantaneous torque deviation from it at those instants is minimum. In such a case, the SCL is still minimized at the instants (if any) of the fundamental period where the torque reference is feasible, preserving the FRML feature. If step b) is applied and it is afterward necessary to limit the resulting peak-to-peak torque ripple to any prespecified value, c) the torque reference is suitably saturated in consecutive samples. The steady-state phase-current rms after overload is also limited to the machine current rating by d) gradually reducing the torque reference. The proposed NSBE-FRML is valid for any phase number, power, OPF/healthy scenario, back-EMF harmonic content, and symmetrical/asymmetrical windings, ensuring its generality. The current references are generated online, without any offline optimization. Thus, the seven aforementioned properties 1)-7) are attained, as indicated in Table I, unlike in the existing publications. Experimental results are obtained with a six-phase PMSM. Compared with the preliminary version presented in [38], features 6) and 7) are added, as well as transient results, assessment of computational burden, tests at other fault scenarios, and so on.

The rest of this article is organized as follows. The existing MTPR technique [23] for setting the current references in *n*-phase PMSMs with nonsinusoidal back EMF while ignoring

the current limits is reviewed in Section II. The overall block diagram of the proposed NSBE-FRML is presented in Section III. The algorithm for minimizing the SCL or torque deviation at each control sample, which is a key part of the method, is explained in Section IV. The schemes for limiting the torque ripple and rms current are described in Sections V and VI, respectively. The experiments are discussed in Section VIII. Finally, the conclusions are summarized in Section VIII.

II. EXISTING CURRENT REFERENCES FOR MINIMUM SCL AND NO CURRENT LIMITS

The MTPR method proposed in [23] is reviewed first. This online general approach generates current references with ripple-free electromagnetic torque and minimum SCL under OPFs without considering the current limits. This technique [23] is equivalent to the ones proposed in other publications [21], [24] for the same purpose. Saliency is neglected [23], because the reluctance torque is normally very small in PMSMs with nonsinusoidal back EMF designed for fault tolerance, such as those with fractional-slot concentrated windings, which offer high decoupling between phases [2], [33], [34]. Similarly, the cogging torque is disregarded as well, since it is also low in these PMSMs when an appropriate slot/pole combination is selected [35], [36].

Let us define a column vector $i = [i_1 \cdots i_n]^T$ formed by the phase currents i_k , with k = 1 for phase a, k = 2 for phase b, and so on. The vector $f = [f_1 \cdots f_n]^T$ contains $f_k = 1$ or $f_k = 0$ for healthy or open phases, respectively, so that $2 \le f^T f \le n$.

The SCL can be minimized by minimizing, at each instant (i.e., per sample), the cost function [23]

$$J = \frac{1}{2} \sum_{k} (i_k)^2 = \frac{1}{2} i^{\mathrm{T}} i.$$
 (1)

To obtain the desired electromagnetic torque T, the equality constraint [23]

$$T = \sum_{k} e_{k} i_{k} = \sum_{k} e_{k}^{\text{nc}} i_{k} = (\mathbf{f} \odot \mathbf{e})^{\text{T}} \mathbf{i}$$
 (2)

should hold, where \odot is elementwise product, e is back EMF over mechanical speed, and $e_k^{\rm nc} = f_k e_k$. Note that e and e i may have any harmonics or imbalance. The e waveform may simply be stored in a lookup table depending on the position if the effect of magnetic saturation and temperature is disregarded [23]; otherwise, an e observer [39], [40] may be used. Another equality constraint to take into account is that, for a single isolated neutral point (which allows high postfault performance [11]), the phase-current sum (zero sequence) is null, i.e., e is e in e i

$$\mathcal{L} = \frac{1}{2} \mathbf{i}^{\mathrm{T}} \mathbf{i} + \lambda_{1} \left(T - (\mathbf{f} \circ \mathbf{e})^{\mathrm{T}} \mathbf{i} \right) + \lambda_{2} \left(\mathbf{f}^{\mathrm{T}} \mathbf{i} \right)$$
(3)

where λ denotes the Lagrange multipliers. To minimize J while satisfying the two aforesaid constraints [included in (3)],

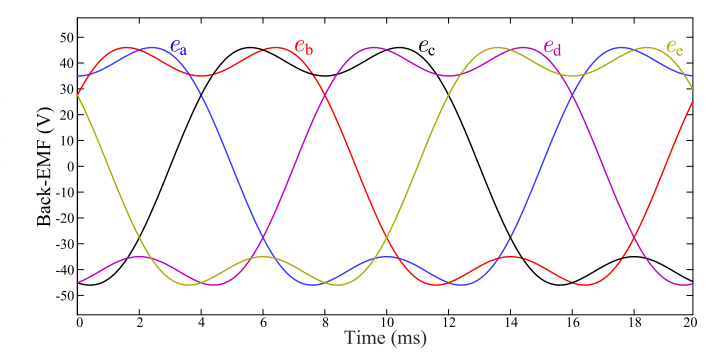


Fig. 4. Example of five-phase back EMF to illustrate the theoretical principles of the methods through simulation.

the partial derivatives of \mathcal{L} with respect to the phase currents and Lagrange multipliers should be zero

$$0 = \mathbf{i} - \lambda_1 \mathbf{f} \circ \mathbf{e} + \lambda_2 \mathbf{f} \tag{4}$$

$$0 = T - (\mathbf{f} \circ \mathbf{e})^{\mathrm{T}} \mathbf{i} \tag{5}$$

$$0 = \boldsymbol{f}^{\mathrm{T}} \boldsymbol{i}. \tag{6}$$

The solution of this system of equations is [23]

$$i = \frac{f \circ e - \frac{f^{\mathsf{T}} e}{f^{\mathsf{T}} f} f}{(f \circ e)^{\mathsf{T}} e - \frac{(f^{\mathsf{T}} e)^{2}}{f^{\mathsf{T}} f}} T \tag{7}$$

which can be computed by 3n-3 additions, n+1 subtractions, 5n+2 multiplications, and one division. If e contains harmonics or if there are OPFs, the resulting current references i are not sinusoidal. Closed-loop current control able to track nonsinusoidal references should be adopted, such as hysteresis [23], [24], finite-control-set model predictive [16], deadbeat [41], [42], or multiresonant [21] current control. However, since the phase-current limits are ignored in the optimization, FRML is not achieved when i is set using (7). Namely, the torque T cannot be raised anymore if any of the phase currents reaches its rating [23].

As an example, a five-phase PMSM without saliency and with the back EMF shown in Fig. 4 is considered. The phase number is set to n = 5 in this example instead of higher values for the sake of simplicity and without loss of generality. The per-phase back-EMF waveform, which is arbitrarily shaped, contains just a third-order harmonic with amplitude equal to 30% of the fundamental one, and with opposite phase angle. For this PMSM, it is, henceforth, assumed that the limits of the instantaneous peak current and of the rms current are i_{pk}^{mx} = 1 A and $i_{\text{rms}}^{\text{mx}} = 0.83$ A, respectively, and that the rated torque is 152.7 Nm. The last two ratings follow from considering $i_{\rm pk}^{\rm mx} = 1 \, {\rm A}$ in healthy conditions. The current references obtained with this method [23] [see (7)] by simulation for the back EMF from Fig. 4, phase a open, and two different T values are shown in Fig. 5. Note that the current waveforms are rescaled with T, according to (7). For the peak-current limit of $i_{\rm pk}^{\rm mx}=1$ A, reaching T=100 Nm (solid) would cause overcurrent ($|i|>i_{\rm pk}^{\rm mx}$), and the maximum admissible torque would be $T_1=75.5$ Nm (dashed-dotted). A new method should be sought to extend the T range.

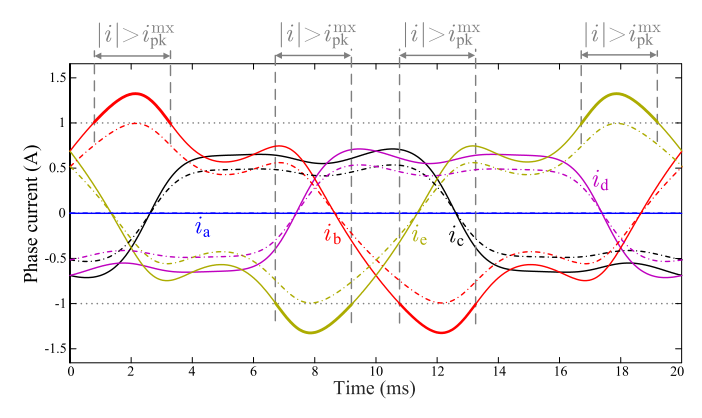


Fig. 5. Current references generated by the method from [23], for the back EMF shown in Fig. 4, phase a open, and torque reference $T=100~\mathrm{Nm}$ (solid) or $T=75.5~\mathrm{Nm}$ (dashed-dotted). The maximum torque with this method would be $T_1=75.5~\mathrm{Nm}$ if the peak-current limit is $t_\mathrm{pk}^\mathrm{mx}=1~\mathrm{A}$.

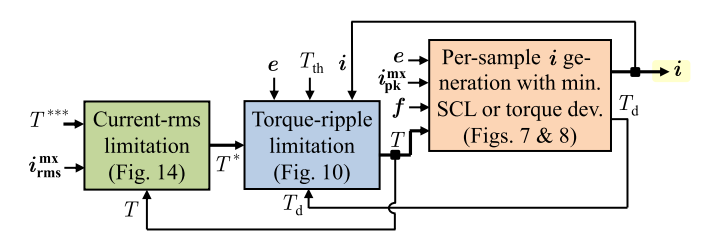


Fig. 6. Overall block diagram of the proposed NSBE-FRML method for current-reference generation.

III. GENERAL OVERVIEW OF THE PROPOSED NSBE-FRML METHOD

Fig. 6 depicts a block diagram of the complete proposed NSBE-FRML method for current-reference generation, which implements the concept from Fig. 3. A MATLAB/Simulink implementation of this scheme is available for download as Supplementary Material of this article. The three blocks included in Fig. 6 are novel. The color of each of these blocks is chosen so as to indicate the relation with those in Fig. 3, as will be done, henceforth, in other block diagrams.

As shown in Fig. 6, the original torque reference T^{***} priorly set externally, is used as an input of the method. In the green (leftmost) block, in case a phase-current rms exceeds its rating $i_{\rm rms}^{\rm mx}$, the torque reference T^* is gradually reduced $(|T^*| \le |T^{***}|)$ with slow dynamics to prevent overheating in steady state, after transient overload. In the blue block, the torque reference is further saturated ($|T| \leq |T^*|$) if necessary, so that, in consecutive samples within a fundamental period, the torque ripple does not surpass its threshold $T_{\rm th}$. In the orange block, which is by far the most important one, the current references are computed on a per-sample basis, so that, while respecting the maximum peak current i_{pk}^{mx} , minimum SCL (if T is feasible) or torque deviation (if T is unfeasible) is achieved. The existence or not of torque deviation from the reference T is indicated by $T_d = 1$ or $T_d = 0$, respectively. Although the green and blue blocks do not perform any action in many cases, the orange block is always needed. Each of these three blocks from Fig. 6, following the order from right to left (to facilitate understanding), is explained in Sections IV-VI, respectively.

TABLE II
INPUTS OF THE ALGORITHM FOR EXAMPLES 1 AND 2 FROM FIG. 9(b)

Variable	T (Nm)	$i_{ m pk}^{ m mx}$ (A)			e (V	7)			\overline{f}
\overline{k}	-	1-5	1	2	3	4	5	1	2-5
Example 1 Example 2	100 100	1	39 45	44 45		$-39 \\ -35$	0 -30	0	1

IV. PROPOSED PER-SAMPLE CURRENT-REFERENCE GENERATION WITH MINIMUM SCL AND TORQUE DEVIATION INCLUDING PEAK-CURRENT LIMITATION

A. General Principle

The method presented in [23] (see Section II) ensures minimum SCL and no torque ripple (smooth electromagnetic torque) as long as the required currents do not reach the drive current limits, which were not taken into account in the optimization problem. As soon as one phase current hits its threshold, the torque reference is saturated, or torque ripple is permitted [23]. However, it might be possible to restrict the highest phase currents to their limits while allowing greater ripple-free torque by increasing the other phase currents with minimum SCL, analogously (but suitably adapted) to the FRML strategy for sinusoidal back EMF [13], [14], [15], [16]. Moreover, when the torque reference is unfeasible (reaching it would imply overcurrent), the references could be set for minimum torque deviation. A technique is proposed here for these purposes, which corresponds to the orange block from Fig. 6. As aforesaid, this crucial block minimizes the instantaneous SCL (if T is feasible) or torque deviation (if T is unfeasible) while respecting the maximum admissible peak of the instantaneous current (average per switching period), denoted as $i_{k,\mathrm{pk}}^{\mathrm{mx}}$ for each phase, with $i_{\mathrm{pk}}^{\mathrm{mx}} = [i_{1,\mathrm{pk}}^{\mathrm{mx}} \cdots i_{n,\mathrm{pk}}^{\mathrm{mx}}]^{\mathrm{T}}$. Typically, $i_{k,\mathrm{pk}}^{\mathrm{mx}}$ equals the switch current rating $i_{\mathrm{pk}}^{\mathrm{mx}}$ for all

This part of the algorithm (orange block from Fig. 6) is detailed in Figs. 7 and 8, with the latter representing a function called in the former. The current references obtained by this algorithm for the back EMF from Fig. 4, phase a open, $i_{pk}^{mx} =$ 1 A, and torque reference T = 80 Nm and T = 100 Nm are shown in Fig. 9(a) and (b), respectively. The torque associated with the resulting current references $T_{\rm f}$, the original torque reference T, and the variable indicating torque deviation T_d are also included. Note that $T_{\rm d}=0$ and $T_{\rm d}=1$ when $T_{\rm f}=T$ and $T_f \neq T$, respectively. It may also be seen that, unlike for conventional MTPR and MTPP, the current waveforms are not simply rescaled with T. At the instants where none of the currents reaches $i_{\rm pk}^{\rm mx}$, the solid current waveforms in Figs. 5 and 9 match. Most importantly, high torque T > $T_1 = 75.5$ Nm is achieved in Fig. 9 without overcurrent in any phase $(|i| \le i_{pk}^{mx})$, unlike for the conventional MTPR method (see Fig. 5). The samples of two representative instants of Fig. 9(b) are labeled as Examples 1 and 2, which will be used for illustrating the explanation of the method subsequently. The corresponding back-EMF values from Fig. 4, as well as the other inputs of the algorithm, are reflected in Table II.

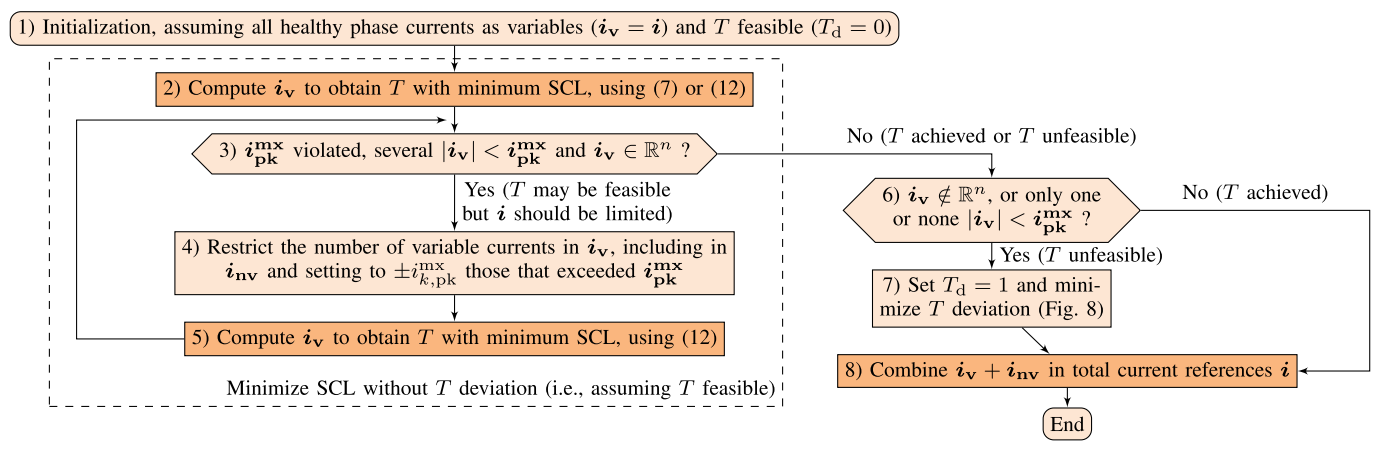


Fig. 7. General flowchart of the per-sample algorithm described in Section IV for current-reference generation with minimum SCL (if *T* is feasible) or torque deviation (if *T* is unfeasible) and with peak-current limitation.

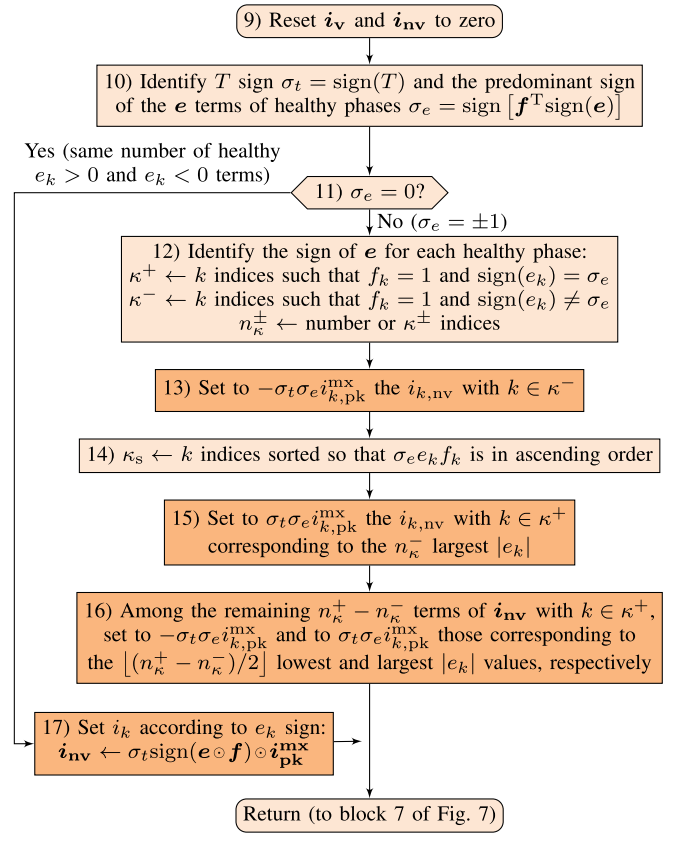


Fig. 8. Detailed per-sample algorithm (contained in block 7 from Fig. 7) described in Section IV-C for current-reference generation with minimum torque deviation (if T is unfeasible, i.e., $T_{\rm d}=1$) and with peak-current limitation.

For the control samples corresponding to Examples 1 and 2, Tables III and IV display, respectively, the values of the main variables as the program runs through the blocks from Figs. 7 and 8.

The proposed method depicted in Figs. 7 and 8 is based on separating the currents of healthy phases, at each sample, between some (those below $i_{k,\mathrm{pk}}^{\mathrm{mx}}$) that are considered as variables for the SCL minimization and some (which tend to surpass $i_{k,\mathrm{pk}}^{\mathrm{mx}}$, and are saturated to it) that are not. The column

vectors $f_{\rm v}$ and $f_{\rm nv}$ indicate the phases corresponding to these two sets, respectively, by means of ones in the associated positions k, while their other elements are zero. Thus, the variable and nonvariable phase currents are $i_{\rm v}=f_{\rm v}\odot i$ and $i_{\rm nv}=f_{\rm nv}\odot i$.

The following explanation of the diagram from Fig. 7 can be studied with the help of the numerical examples of Tables III and IV. Initially, in block 1 of Fig. 7, all healthy phase currents are regarded as degrees of freedom in i_v (f_v = f and $f_{nv} = 0f$). This means that the optimum currents are calculated first (block 2) by ignoring the current limits, as in (7), with $i = i_v$. Then, it is checked (block 3) if any of the obtained phase currents i_k in i_v exceed (violate) $i_{k \text{ nk}}^{\text{mx}}$ in absolute value. If some of them do, they are included in i_{nv} and limited (set) to $\pm i_{k,pk}^{mx}$ in the next step (block 4), keeping the respective sign. Accordingly, the associated positions of $f_{\rm v}$ and $f_{\rm nv}$ are set to 0 and 1, respectively. Then, the optimum $i_{\rm v}$ currents providing the torque reference T with minimum SCL are calculated with these new conditions, in block 5. This optimization cannot be achieved through (7), where all healthy phase currents were considered as degrees of freedom. The necessary equations for this optimization are derived shortly, in Section IV-B. After this computation, as shown in Fig. 7, the process (blocks 3–5) is iteratively repeated, until at least one of the following three conditions occurs in block 3.

- 1) No $|i_v|$ values exceed i_{pk}^{mx} .
- 2) Just one or none of the $|i_v|$ values is/are below $i_{\rm pk}^{\rm mx}$.
- 3) Some i_v terms are infinite or indeterminate $(i_v \notin \mathbb{R}^n)$. If 1) is true and not 2) nor 3), T is achieved without overcur-

rent ($T_d = 0$ and $T_f = T$), and the resulting i_v and i_{nv} may already be combined to give suitable total current references i, as done in block 8, reached in this case through the rightmost path. Example 1 corresponds to this case, as can be observed in Table III, whose final values match those indicated in Fig. 9(b). This is also the case for all of the instants in Fig. 9(a), where T_f always matches T without deviation, avoiding torque ripple. Otherwise, if 2) or 3) happens, as in Example 2 (see Table IV), it can be concluded that T is unfeasible [$T_d = 1$ and $T_f \neq T$, as in Fig. 9(b)], and the currents are then set in block 7, so that the torque deviation from its reference is minimum, while respecting i_{pk}^{mx} and (6).

TABLE III EXAMPLE 1 OF EXECUTION OF THE SCHEME FROM FIG. 7 FOR n=5 AT A CERTAIN CONTROL SAMPLE WITH THE INPUTS SHOWN IN TABLE II

Variable			$f_{ m v}$					$f_{ m n}$	v				$i_{\mathbf{v}}$ (2	4)			$i_{ m r}$	ıv ((A)		σ_t	σ_e	κ^+	κ^-	n_{κ}^{+}	n_{κ}^{-}	$\kappa_{ m s}$			i ((A)	
\overline{k}	1	2	3	4	5	1	2	3	4	5	1	2	3	4	5	1	2	3	4	5	-	-	-	-	-	-	-	1	2	3	4	5
Block 1	0	1	1	1	1	0	0	0	0	0	0	0	0	0	0	0	0	0	0	0	-	-	-	-	-	-	-	-	-	-	-	-
Block 3	0	1	1	1	1	0	0	0	0	0	0	1.07	-0.68	-0.58	0.19	0	0	0	0	0	-	-	-	-	-	-	-	-	-	-	-	-
Block 4	0	0	1	1	1	0	1	0	0	0	0	1.07	-0.68	-0.58	0.19	0	1	0	0	0	-	-	-	-	-	-	-	-	-	-	-	-
Block 5	0	0	1	1	1	0	1	0	0	0	0	0	-0.73	-0.61	0.34	0	1	0	0	0	-	-	-	-	-	-	-	-	-	-	-	-
Block 8	0	0	1	1	1	0	1	0	0	0	0	0	-0.73	-0.61	0.34	0	1	0	0	0	-	-	-	-	-	-	-	0	1	-0.73	-0.61	0.34

TABLE IV EXAMPLE 2 OF EXECUTION OF THE SCHEME FROM FIGS. 7 AND 8 FOR n=5 AT A CERTAIN CONTROL SAMPLE WITH THE INPUTS SHOWN IN TABLE II

Variable			$f_{ m v}$					f_1	av					$i_{ m v}$ ((A)				$i_{ m nv}$	(A)		σ_t	σ_e	κ^+	κ^-	n_{κ}^{+}	n_{κ}^{-}	$\kappa_{ m s}$			i ((A)	
\overline{k}	1	2	3	4	5	1	2		3	4	5	1	2	3	4	5	1	2	3	4	5	-	-	-	-	-	-	-	1	2	3	4	5
Block 1	0	1	1	1	1	0	0	())	0	0	0	0	0	0	0	0	0	0	0	-	-	-	-	-	-	-	-	-	-	-	-
Block 3	0	1	1	1	1	0	0	())	0	0	1.32	-0.32	-0.56	-0.44	0	0	0	0	0	-	-	-	-	-	-	-	-	-	-	-	-
Block 4	0	0	1	1	1	0	1	())	0	0	1.32	-0.32	-0.56	-0.44	0	1	0	0	0	-	-	-	-	-	-	-	-	-	-	-	-
Block 5	0	0	1	1	1	0	1	())	0	0	0	2.17	-2.83	-0.33	0	1	0	0	0	-	-	-	-	-	-	-	-	-	-	-	-
Block 12	0	0	1	1	1	0	1	())	0	0	0	0	0	0	0	0	0	0	0	1	-1	345	2	3	1	-	-	-	-	-	-
Block 14	0	0	1	1	1	0	1	())	0	0	0	0	0	0	0	1	0	0	0	1	-1	345	2	3	1	12354	-	-	-	-	-
Block 15	0	0	1	1	1	0	1	())	0	0	0	0	0	0	0	1	0	-1	0	1	-1	345	2	3	1	12354	_	-	-	-	_
Block 16	0	0	1	1	1	0	1	())	0	0	0	0	0	0	0	1	1	-1	-1	1	-1	345	2	3	1	12354	_	-	-	-	_
Block 8	0	0	1	1	1	0	1	())	0	0	0	0	0	0	0	1	1	-1	-1	1	-1	345	2	3	1	12354	0	1	1	-1	-1

In short, for each sample, if T is feasible, the currents producing T with minimum SCL are found in blocks 2–5 of Fig. 7 (equations in Section IV-B), and otherwise, the currents providing minimum deviation from T are obtained in block 7, which calls the function detailed in Fig. 8 (explained in Section IV-C).

B. Equations of i_v for Providing T With Minimum SCL While Limiting i_{nv}

The equations needed for computing the optimum i_v to yield T with minimum SCL while limiting i_{nv} (blocks 2 and 5 of Fig. 7) are derived next. Using the new variables from Section IV-A, (3) may be rewritten as follows:

$$\mathcal{L} = \frac{1}{2} i_{\mathbf{v}}^{\mathsf{T}} i_{\mathbf{v}} + \frac{1}{2} i_{\mathbf{n}\mathbf{v}}^{\mathsf{T}} i_{\mathbf{n}\mathbf{v}} + \lambda_2 (f_{\mathbf{v}}^{\mathsf{T}} i_{\mathbf{v}} + f_{\mathbf{n}\mathbf{v}}^{\mathsf{T}} i_{\mathbf{n}\mathbf{v}}) + \lambda_1 (T - (f_{\mathbf{v}} \circ \mathbf{e})^{\mathsf{T}} i_{\mathbf{v}} - (f_{\mathbf{n}\mathbf{v}} \circ \mathbf{e})^{\mathsf{T}} i_{\mathbf{n}\mathbf{v}}).$$
(8)

Analogously to (4)–(6), equating to zero the partial derivatives of (8) with respect to the current variables and Lagrange multipliers yields

$$0 = \mathbf{i}_{\mathbf{v}} - \lambda_1 \mathbf{f}_{\mathbf{v}} \circ \mathbf{e} + \lambda_2 \mathbf{f}_{\mathbf{v}} \tag{9}$$

$$0 = T - (\mathbf{f}_{\mathbf{v}} \odot \mathbf{e})^{\mathrm{T}} \mathbf{i}_{\mathbf{v}} - (\mathbf{f}_{\mathbf{n}\mathbf{v}} \odot \mathbf{e})^{\mathrm{T}} \mathbf{i}_{\mathbf{n}\mathbf{v}}$$
(10)

$$0 = f_{\mathbf{v}}^{\mathsf{T}} i_{\mathbf{v}} + f_{\mathbf{n}\mathbf{v}}^{\mathsf{T}} i_{\mathbf{n}\mathbf{v}}. \tag{11}$$

Solving this system gives

$$i_{\mathbf{v}} = \frac{f_{\mathbf{v}} \circ \mathbf{e} - \frac{f_{\mathbf{v}}^{\mathsf{T}} \mathbf{e}}{f_{\mathbf{v}}^{\mathsf{T}} f_{\mathbf{v}}} f_{\mathbf{v}}}{(f_{\mathbf{v}} \circ \mathbf{e})^{\mathsf{T}} \mathbf{e} - \frac{(f_{\mathbf{v}}^{\mathsf{T}} \mathbf{e})^{2}}{f_{\mathbf{v}}^{\mathsf{T}} f_{\mathbf{v}}}} (T - T_{\mathsf{nv}}) - \frac{f_{\mathsf{nv}}^{\mathsf{T}} i_{\mathsf{nv}}}{f_{\mathbf{v}}^{\mathsf{T}} f_{\mathbf{v}}} f_{\mathbf{v}}$$
(12)

where

$$T_{\text{nv}} = (\mathbf{f}_{\text{nv}} \odot \mathbf{e})^{\text{T}} \mathbf{i}_{\text{nv}} - (\mathbf{f}_{\text{v}} \odot \mathbf{e})^{\text{T}} \mathbf{f}_{\text{v}} \frac{\mathbf{f}_{\text{nv}}^{\text{T}} \mathbf{i}_{\text{nv}}}{\mathbf{f}_{\text{v}}^{\text{T}} \mathbf{f}_{\text{v}}}.$$
 (13)

Setting $f_v = f$ and $f_{nv} = 0f$ in (12), ignoring the current limits, results in (7). Equation (12) is employed in blocks 2 and 5 of Fig. 7 in order to compute i_v . Note that all denominators are scalar, and no matrix inversions are needed. The i_v computation using (12) and (13) needs 6n-6 additions, 2n+3 subtractions, 10n+2 multiplications, and two divisions.

C. Minimization of Torque Deviation When T Is Unfeasible

When T cannot be achieved without violating i_{pk}^{mx} , the main objective becomes minimizing the torque deviation, i.e., $T - T_f$. This is equivalent to maximizing the torque T_f in absolute value, with sign $\sigma_t = \text{sign}(T)$, where the function sign(u), in general, returns +1, -1, or 0 for positive, negative, or null values of the input u, respectively. For this goal, the procedure in Fig. 8 is applied. Example 2 [see Table IV and the corresponding values in Fig. 9(b)] is helpful for understanding this part of the algorithm. The main idea is based on setting all phase currents to the maximum value and with signs equal to those of the corresponding phase back EMFs, or if not possible, at least in those phases with the largest back EMF.

First, $i_{\mathbf{v}}$ and $i_{\mathbf{n}\mathbf{v}}$ are reset to zero in block 9. The former will be kept null. $f_{\mathbf{v}}$ and $f_{\mathbf{n}\mathbf{v}}$ are not needed anymore. It is then identified in block 10, by means of the new variable $\sigma_e = \text{sign}[f^T \text{sign}(e)]$, if most of the e_k values of healthy phases are positive ($\sigma_e = +1$) or negative ($\sigma_e = -1$), or if there is the same number of positive and negative healthy e_k terms ($\sigma_e = 0$). In the latter case, T is maximized by simply setting all the $i_{\mathbf{n}\mathbf{v}}$ values of healthy phases to $i_{k,\mathbf{p}k}^{mx}$, with sign equal to the product of the T and e_k signs (block 17). Otherwise (if $\sigma_e \neq 0$), special care should be paid to ensure that (11) is satisfied, by taking several steps. The indices of the healthy phases with e_k signs equal and different from σ_e are saved as κ_+ and κ_- , respectively, whose numbers are n_k^+

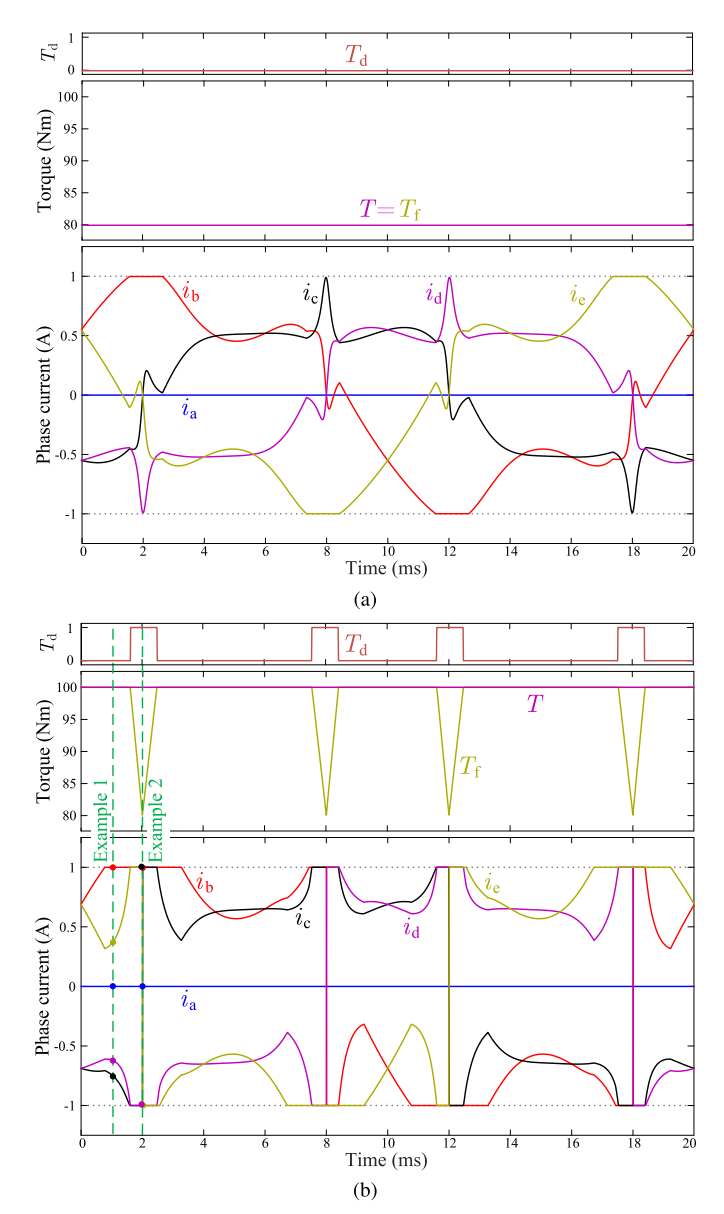


Fig. 9. Current references generated by the proposed algorithm from Figs. 7 and 8, as well as the corresponding torque $T_{\rm f}$ and variable $T_{\rm d}$, for the back EMF shown in Fig. 4, phase a open, peak-current limit $i_{\rm pk}^{\rm mx}=1$ A, and torque reference (a) T=80 Nm or (b) T=100 Nm.

and n_{κ}^{-} (block 12). For instance, for the e vector considered in Table IV (detailed in the last row of Table II), three of its elements corresponding to healthy phases are positive and one negative, such that $\sigma_e = +1$, $\kappa_+ = \{3, 4, 5\}$, $\kappa_- = \{2\}$, $n_{\kappa}^{+}=3$, and $n_{\kappa}^{-}=1$, as indicated in Table IV. Then, all the i_{nv} terms with $k \in \kappa_{-}$ are set to $i_{k,pk}^{mx}$ with sign $-\sigma_{t}\sigma_{e}$ in block 13, maximizing their contribution to the torque. However, not all the currents with $k \in \kappa_+$ can be set with sign $\sigma_t \sigma_e$, because (11) would be infringed. Thus, it is useful to establish, among the e_k values with $k \in \kappa_+$, those that are the highest, which offer the greatest potential to increase the torque. Accordingly, the indices are sorted in κ_s (block 14), so that the $\sigma_e e_k f_k$ values are in ascending order. Then, i_{nv} is set to $\sigma_t \sigma_e i_{k.nk}^{mx}$ for the n_{κ}^- highest indices in κ_s (with $k \in \kappa_+$) in block 15, yielding as large torque as possible while canceling the zerosequence current produced by the n_{κ}^- phases with $k \in \kappa_-$.

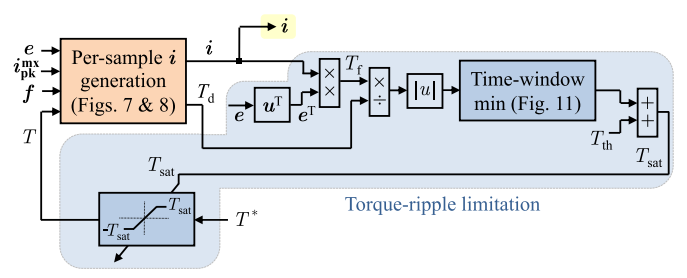


Fig. 10. Within the scheme of the proposed NSBE-FRML method (from Fig. 6), detailed block diagram of the algorithm described in Section V for limiting the torque ripple by T saturation in consecutive samples (blue-shaded area).

Among the remaining $n_k^+ - n_k^-$ elements of i_{nv} with $k \in \kappa^+$, those corresponding to the $\lfloor (n_k^+ - n_k^-)/2 \rfloor$ lowest and largest $|e_k|$ terms are set to $-\sigma_t \sigma_e i_{k,pk}^{mx}$ and to $\sigma_t \sigma_e i_{k,pk}^{mx}$, respectively, in block 16. In this manner, the sum of the former current set is canceled with the sum of the latter in the zero sequence (11), with maximum torque production as well. To recapitulate, the torque deviation is minimized by maximizing the torque, which, in turn, is done by setting the phase currents to $i_{k,pk}^{mx}$ and with signs matching those of e_k in all the phases, or if it cannot be done with null zero-sequence current, at least in the phases with greatest back EMF.

As illustrated in Fig. 9(b), in Example 2, the currents of all the healthy phases are made equal to the peak-current limit to minimize the torque deviation $T - T_f$. In any case, the torque drop that happens at this instant gives rise to some torque ripple during the fundamental period. For instance, in Fig. 9(b), this ripple is of 20 Nm. The limitation of this torque oscillation is the focus of Section V.

V. PROPOSED LIMITATION OF TORQUE RIPPLE BY T SATURATION IN CONSECUTIVE SAMPLES

The method proposed in Section IV (Figs. 7 and 8) provides, in each sampling period, optimum current references with minimum SCL and no torque deviation from T ($T_d = 0$), i.e., $T = T_f$, or if this is unfeasible $(T_d = 1)$, the lowest Tdeviation $T - T_f$. Nonetheless, if the latter condition $(T_d = 1)$ occurs at some point of the fundamental period, certain ripple arises in the electromagnetic torque [as in Fig. 9(b)], and it may be excessive in some cases, if it surpasses the acceptable peak-to-peak threshold T_{th} . T_{th} may be defined depending on the allowable vibrations and acoustic noise for the application at hand [43], deducting the expected switching ripple and cogging torque (if not negligible) [42]. The torque pulsation can be limited to T_{th} by adequately reducing (saturating) the reference T in consecutive samples by the scheme shown in the blue-shaded area of Fig. 10, where T^* is the torque reference before its saturation.

In Fig. 10, first, the final torque T_f provided by the currents obtained from Figs. 7 and 8 is found by using (2): $T_f = e^T i$. Its absolute value is computed after division by T_d , yielding infinite or $|T_f|$ depending on whether T_f equals T or not, respectively. Then, the minimum of this signal within the most recent time interval (window) of a certain length t_w is calculated. This represents the smallest torque $|T_f|$ different

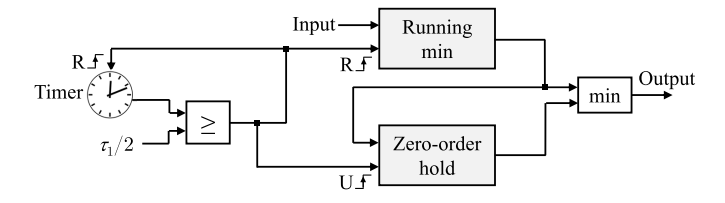


Fig. 11. Block diagram of time-window minimum function for Fig. 10.

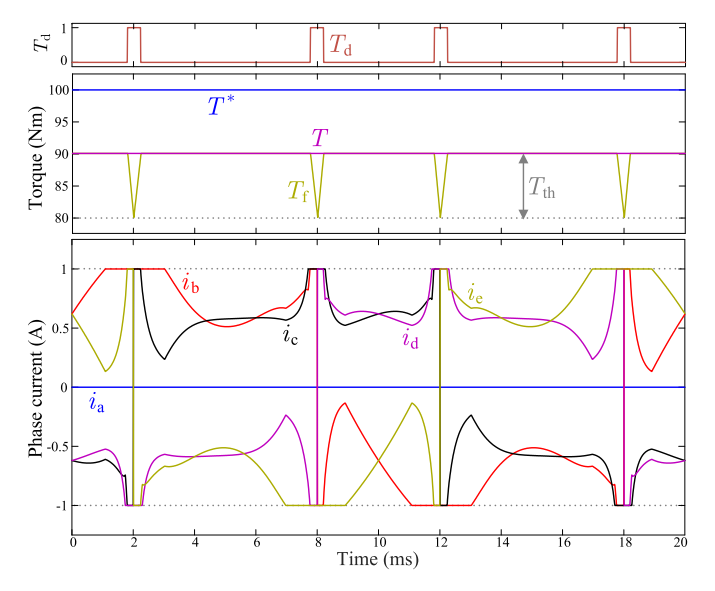


Fig. 12. Current references generated by the proposed scheme from Fig. 10, as well as the corresponding torque $T_{\rm f}$ and variables T and $T_{\rm d}$, for the back EMF shown in Fig. 4, phase a open, peak-current limit $i_{\rm px}^{\rm px}=1$ A, torque reference $T^*=100$ Nm, and torque-ripple threshold $T_{\rm th}=10$ Nm.

from T (when unfeasible) during such interval. This quantity is added to T_{th} giving T_{sat} , to which T should be saturated in the following sample in order to limit the torque ripple to T_{th} .

The aforesaid time-window minimum may be performed, as shown in Fig. 11, where a running minimum function is reset (R) every $\tau_1/2$ (with τ_1 being the fundamental period), a zero-order hold of its output is updated (U) at the same moments, and the minimum of both block outputs is computed at every instant. In this manner, t_w varies between $\tau_1/2$ and τ_1 , which is simpler to implement than a sliding-window minimum with constant t_w . Note that, due to symmetry, in steady state, the |e|, |i|, and T_f waveforms are repeated every $\tau_1/2$ cycle.

It should be remarked that this algorithm works effectively even if it is decided to vary T_{th} depending on the operating conditions (e.g., speed) or to set it to zero at all times.

Fig. 12 shows the signals obtained by means of the method from Fig. 10 for the same scenario as in Fig. 9(b), but considering a torque-ripple limitation to $T_{\rm th}=10\,{\rm Nm}$. The torque reference of 100 Nm is now set using T^* , since this is the one used as an input in Fig. 10. It can be observed that in this case, the torque pulsation is effectively reduced from $100-80=20\,{\rm Nm}$ [Fig. 9(b)] to $90-80=10\,{\rm Nm}$ (Fig. 12) because of the saturation of $T^*=100\,{\rm Nm}$ to $T=T_{\rm sat}=90\,{\rm Nm}$ provided by the algorithm. Note that the resulting torque is still substantially larger than the maximum with the conventional method, $T_1=75.5\,{\rm Nm}$ (see Fig. 5).

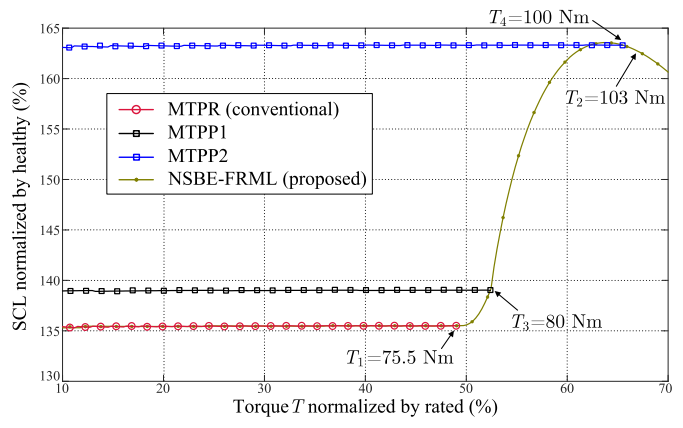


Fig. 13. SCL versus torque T for the conventional MTPR method [23], the proposed scheme, and MTPP methods obtained by rescaling the current waveforms of $T_3 = 80 \text{ Nm}$ or $T_4 = 100 \text{ Nm}$ ($T_{th} = 20 \text{ Nm}$), for the back EMF shown in Fig. 4, phase a open, and peak-current limit $t_{pk}^{\text{mx}} = 1 \text{ A}$.

In accordance with Fig. 10, $T_{\rm sat} = 90 \,\mathrm{Nm}$ is obtained in Fig. 12 by adding $T_{\rm th} = 10 \,\mathrm{Nm}$ to the minimum of $T_{\rm f}$, which is 80 Nm. In general, the highest admissible T with $T_{\rm f}$ ripple below $T_{\rm th}$ is $T_4 = T_{\rm sat} = T_3 + T_{\rm th}$, with T_3 being the greatest T without any $T_{\rm f}$ pulsation, which coincides with the minimum $T_{\rm f}$ of the torque oscillations when they arise, as in Fig. 12 $(T_3 = 80 \,\mathrm{Nm})$.

Table V summarizes the main characteristics of the performance of the proposal with different T values for the example under study. The p.u. values of peak current, rms current, SCL, and T are normalized by $i_{pk}^{mx} = 1 \text{ A}$, $i_{rms}^{mx} = 0.83 \text{ A}$, $5(i_{rms}^{mx})^2$, and 152.7 Nm, respectively (see Section II). When $T \leq T_1$, the new method matches the conventional one [23] reviewed in Section II, because $|i| < i_{pk}^{mx}$. In addition, Fig. 13 represents the relation between the normalized SCL and the torque reference T of the new technique, compared with the conventional MTPR from [23] and MTPP methods (MTPP1 and MTPP2) obtained by rescaling with T the current waveforms of the proposal corresponding to $T_2 = 80 \text{ Nm}$ or $T_4 = 100 \text{ Nm}$ $(T_{\rm th}=20\,{\rm Nm})$. It can be seen in these simulation results that the proposed strategy attains FRML behavior, as intended: it extends the torque range well beyond the maximum of MTPR T_1 , and the SCL for each T value is minimum (below MTPP, and matching MTPR for $T \leq T_1$). In any case, the MTPP associated with T_4 (MTPP2) may be discarded in practice, because it would give rise to torque ripple even at low load; indeed, since MTPP2 simply rescales the T_4 current waveforms by T/T_4 , the torque pulsation corresponding to T_4 [see Fig. 9(b)] is also just rescaled by the same factor instead of being canceled. Thus, only the proposal ensures FRML and minimum torque ripple.

The proposed method is able to reach T higher than 100 Nm; however, it can be observed in Table V that, for $T > T_2 = 103$ Nm, the current in some (at least two) phases surpasses $i_{\rm rms}^{\rm mx}$. This occurs, e.g., for $T_4 = 110$ Nm, which is allowed if $T_{\rm th} = 30$ Nm. The phase-current rms excess for $T > T_2$ can be accepted during transient overload, but it could cause machine overheating (e.g., hot spots [1], [10], [11]) if it is kept for excessive time. This aspect is addressed in Section VI.

(T. (N.))	/TI (-)	Description	Torque ri-	Peak cu-	rms curre		CCI ()
T (Nm)	T (p.u.)	Description	pple (Nm)	rrent (p.u.)	k = 2, 5	k = 3, 4	SCL (p.u.)
$< T_1 = 75.5$	< 0.49	$ i_k < i_{\mathrm{pk}}^{\mathrm{mx}}$ for any k (conventional)	0	< 1.0	< 0.74	< 0.53	< 0.33
$T_1 = 75.5$	0.49	Max. T without reaching $i_{\rm pk}^{\rm mx}$ for any k (conventional)	0	≈ 1.0	0.74	0.53	0.33
$T_2 = 103$	0.67	Max. T without exceeding $i_{\text{rms}}^{\text{mx}}$ for any k	23	1.0	1.0	0.92	0.74
$T_3 = 80$	0.52	Max. T without ripple in $T_{\rm f}$	0	1.0	0.78	0.59	0.38
$T_4 = 90 \ (T_{\rm th} = 10)$	0.59	Max. T with $T_{\rm f}$ ripple under $T_{\rm th}=10~{\rm Nm}$	10	1.0	0.90	0.77	0.56
$T_4 = 100 \ (T_{\rm th} = 20)$	0.65	Max. T with $T_{\rm f}$ ripple under $T_{\rm th}=20~{\rm Nm}$	20	1.0	0.98	0.89	0.70
$T_4 = 110 \ (T_{\rm th} = 30)$	0.72	Max. T with $T_{\rm f}$ ripple under $T_{\rm th}=30~{ m Nm}$	30	1.0	1.05	0.99	0.82

TABLE V Performance of the Proposed Method for the Back EMF from Fig. 4, Phase a Open, $i_{\rm nk}^{\rm mx}=1$ A, and $i_{\rm nk}^{\rm rms}=0.83$ A

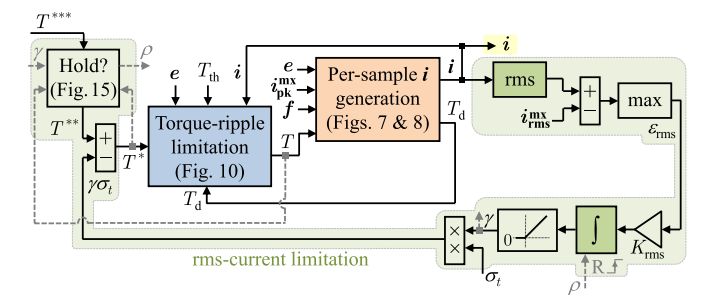


Fig. 14. Scheme of the proposed NSBE-FRML method (from Fig. 6) including the detailed block diagram of the algorithm described in Section VI for limiting the rms current by gradual T reduction (green-shaded area).

VI. PROPOSED LIMITATION OF RMS CURRENT BY GRADUAL T REDUCTION

The maximum rms current $i_{\rm rms}^{\rm mx} = [i_{1,{\rm rms}}^{\rm mx} \cdots i_{n,{\rm rms}}^{\rm mx}]^{\rm T}$ should be respected in every phase after a number of fundamental cycles to prevent machine overheating. For this goal, the blocks in the green-shaded area of Fig. 14 are added, so that the complete proposed scheme is finally obtained.

In the right-hand side of Fig. 14, the rms of each phase current is computed, and the maximum deviation (among the *n* phases) from $i_{\rm rms}^{\rm mx}$ is found, giving $\varepsilon_{\rm rms}$. The limits $i_{\rm rms}^{\rm mx}$ can be set to the rated current of the healthy machine $i_{\rm rms}^{\rm mx}$ in all phases; thereby, although there might be nonuniform temperature distribution in the windings due to i imbalance, it is ensured that in steady state, the temperature is not greater than in healthy rated conditions in any phase, avoiding hot spots [1], [10], [11]. The resulting rms excess $\varepsilon_{\rm rms}$ is integrated through a gain $K_{\rm rms}$, and the output γ is saturated, so that negative values are replaced by zero (see Fig. 14). This factor γ is multiplied by the sign σ_t of the torque reference and then subtracted from it.² In this manner, when any of the phase-current rms values exceed their upper bound, the torque reference is gradually decreased until none of them do. The dynamics of this loop can be set by $K_{\rm rms}$ so as to obtain the desired overload time, which depends on the thermal behavior and is out of the scope of this article.

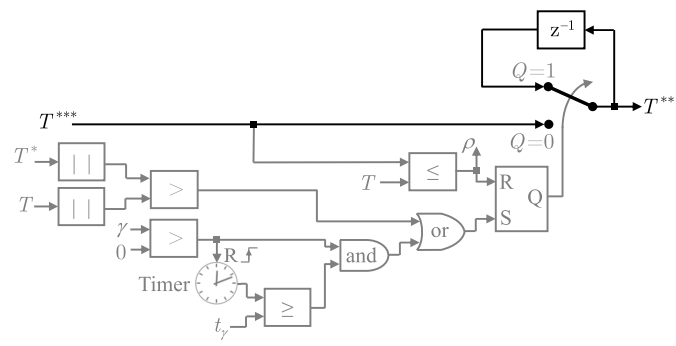


Fig. 15. Block diagram of T^{***} hold function for Fig. 14.

When T^* is saturated by the torque-ripple limitation $(|T^*| > |T|)$, further rise of the original torque reference T^{***} (priorly set externally) is not translated into a T increase, but it may affect the dynamics of the rms-current limitation in Fig. 14. For instance, the integrator may need to generate a very large $\gamma \sigma_t$, and this accumulated value can cause excessive reduction of T once T^{***} returns to a feasible range. To avoid this behavior, the block shown at the top-left corner of Fig. 14 is included, whose content is detailed in Fig. 15. This function begins to hold the T^{***} value in its output T^{**} if there is T^* saturation ($|T^*| > |T|$), or if $\gamma > 0$ for a longer time than a threshold t_{γ} , until T^{***} decreases down to T again. In addition, the latter condition is indicated by setting to one the auxiliary variable ρ , which is also employed to reset the integrator from Fig. 14. Because of these operations, the torque-ripple and rms-current limitation functions can work properly in combination.

For instance, for the example under consideration, if T is greater than $T_2=103$ Nm (see Table V), e.g., T=110 Nm, there is rms-current excess (rms over 1 p.u.) in the two phases adjacent to the faulty one, implying $\varepsilon_{\rm rms}>0$. Consequently, the scheme from Fig. 14 reduces T until it eventually equals $T_2=103$ Nm, so that the largest phase-current rms values are limited to 1 p.u., and thus, $\varepsilon_{\rm rms}=0$.

VII. EXPERIMENTAL RESULTS

A. Experimental Setup and General Description of the Results

The experiments are performed by means of a six-phase surface-mounted PMSM (see Fig. 16) with double-layer fractional-slot concentrated windings and asymmetrical winding arrangement (two three-phase sets displaced by $\pi/6$ [2]).

¹The rms may be calculated using two blocks, one accumulating the squared current and the other performing a zero-order hold, with the former and latter blocks being reset and synchronized with the same signal as in Fig. 11.

 $^{^2}$ A z^{-1} delay may be added at this point (after the subtraction) to avoid algebraic loops.

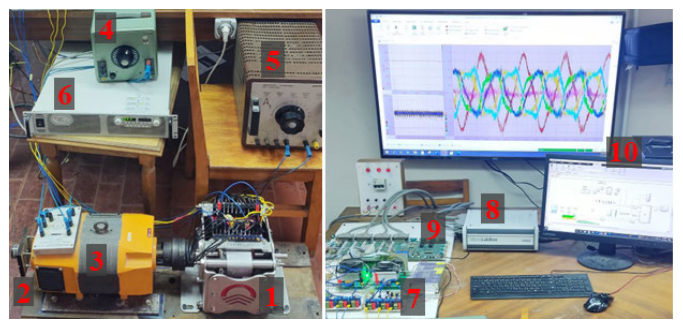


Fig. 16. Experimental setup. 1) Six-phase PMSM. 2) Encoder. 3) DC generator. 4) Generator dc excitation. 5) Loading resistor. 6) DC-link programmable supply. 7) Six-phase inverter. 8) Control platform (dSPACE 1202 MicroLabBox). 9) dSPACE interface board. 10) Host PC (ControlDesk).

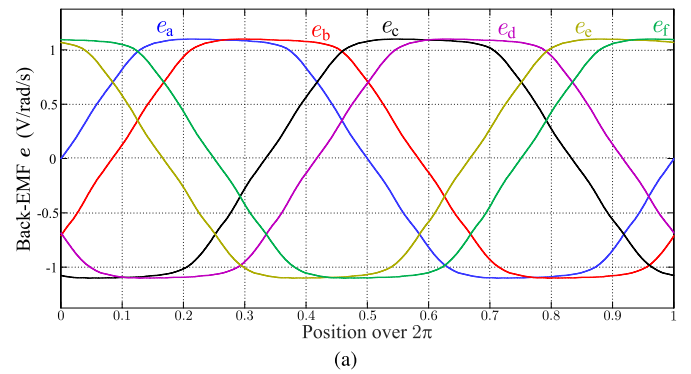
TABLE VI ${\bf Main\ Parameters\ of\ the\ PMSM\ in\ the\ Experimental\ Setup}$

Parameter (unit)	Value
Number of poles	10
Number of slots	12
Rated phase current $i_{\text{rms}}^{\text{mx}}$ (A)	3.2
Rated phase voltage (V)	110
Rated speed (r/min)	1200
Rated torque (Nm)	16.7
Stator inductance in the main $(\alpha-\beta)$ plane (mH)	16.5
Stator leakage inductance in the secondary subspaces (mH)	17.0
Stator resistance (Ω)	1.1

The PMSM parameters are summarized in Table VI. Note that $i_{\text{rms}}^{\text{ims}} = 3.2 \text{ A}$. The back-EMF e signals and their spectrum are shown in Fig. 17. These per-phase waveforms are stored in a lookup table, so that they can be swept based on the position measurement from the encoder [44]. Other details about the PMSM are given in [31].

As shown in Fig. 16, this PMSM is driven by a six-leg voltage-source converter based on IGBTs, with a dc-link voltage of 300 V. It is controlled by a dSPACE 1202 MicroLabBox, using rotor field-oriented control with inner finite-control-set model-predictive current control. The latter is implemented using two-step ahead prediction, the vector-space decomposition, no weighting factors, and only the so-called large voltage vectors [45]. Sampling frequencies of 10 and 50 kHz are used for the current-reference generation and for the model predictive control, respectively. The external torque reference T^{***} (see Fig. 1) is directly set in open-loop manner, without speed control, in order to focus the analysis on the response to T^{***} . The six-phase PMSM is mechanically loaded by a dc generator, which is connected to a variable resistor.

In the following, when expressed in p.u. and unless otherwise said, the torque values are normalized by the rated torque, the rms current is normalized by i_{rms}^{mx} , the SCL is normalized by $6(i_{rms}^{mx})^2$, and the current instantaneous and peak values are normalized by i_{pk}^{mx} , which is assumed to match the peak value of the stator current for the machine rated conditions and healthy drive, i.e., 4.34 A.^3 The experimental torque T_{exp} is estimated based on the measured phase currents using (2), as often done in the literature on the subject [20],



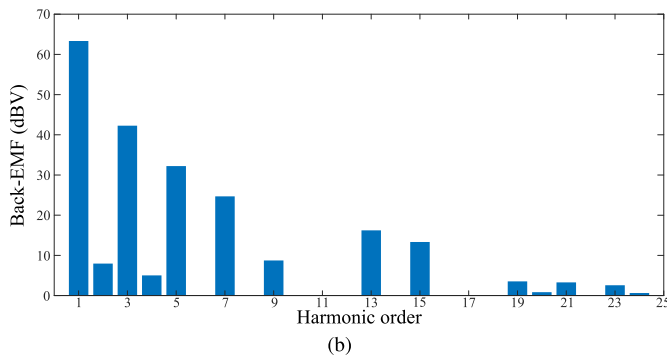


Fig. 17. Back EMF *e* of PMSM for the experimental tests. (a) Per-phase waveforms normalized by speed. (b) Spectrum at rated speed.

[21], [23], [28], [29]. This approach gives a reliable assessment of the torque ripple due to the currents, without the attenuation caused by the reduced bandwidth of torque meters and without the pulsation produced by other sources, such as cogging torque [42]. The peak current is computed in the results after applying a moving-average filter of 0.1 ms to the phase currents in order to attenuate the switching ripple, since the overload time of IGBTs is typically similar or slightly longer. A moving-average filter of 1 ms is used for $T_{\rm exp}$. Unless otherwise said, the tests are performed with phase a open, and setting $T_{\rm th} = 0.12$ p.u. = 2 Nm, $K_{\rm rms} = 1$, and $t_{\gamma} = 5$ s. The results saved by the dSPACE platform are shown rather than oscilloscope captures because of the high number of signals involved, with many of them being internal control variables.

B. Current, Torque, and SCL for Phase a Open

1) Current and Torque for Gradual T^{***} Variation and at Steady State: As shown in Fig. 18, initially, T^{***} is raised progressively up to 16 Nm, while the load resistance of the generator is maintained. After several seconds, T^{***} is reduced again. The other torque-reference signals (T^{***} , T^{**} , and T) used as intermediate steps in the proposed scheme (from Fig. 14), as well as the torque $T_{\rm f}$ (see Fig. 10) produced by the final current references, vary accordingly in Fig. 18. The most relevant T values ($T_{\rm 1}=0.53~{\rm p.u.}$, $T_{\rm 2}=0.67~{\rm p.u.}$, $T_{\rm 3}=0.71~{\rm p.u.}$, and $T_{\rm 4}=0.80~{\rm p.u.}$) are indicated at the top of Fig. 18, and steady-state results (at 600 r/min) corresponding to them are shown in Fig. 19. Some figures of merit for these four steady-state scenarios are summarized in Table VII, where the definitions of $T_{\rm 1}$ – $T_{\rm 4}$ are also recalled. According to these definitions, the values of $T_{\rm 1}$ – $T_{\rm 4}$ are assessed based on the

³It is reasonable to assume that, to optimize the efficiency, a practical drive is designed, so that the switch rated current $i_{\text{nx}}^{\text{mx}}$ satisfies this condition [16].

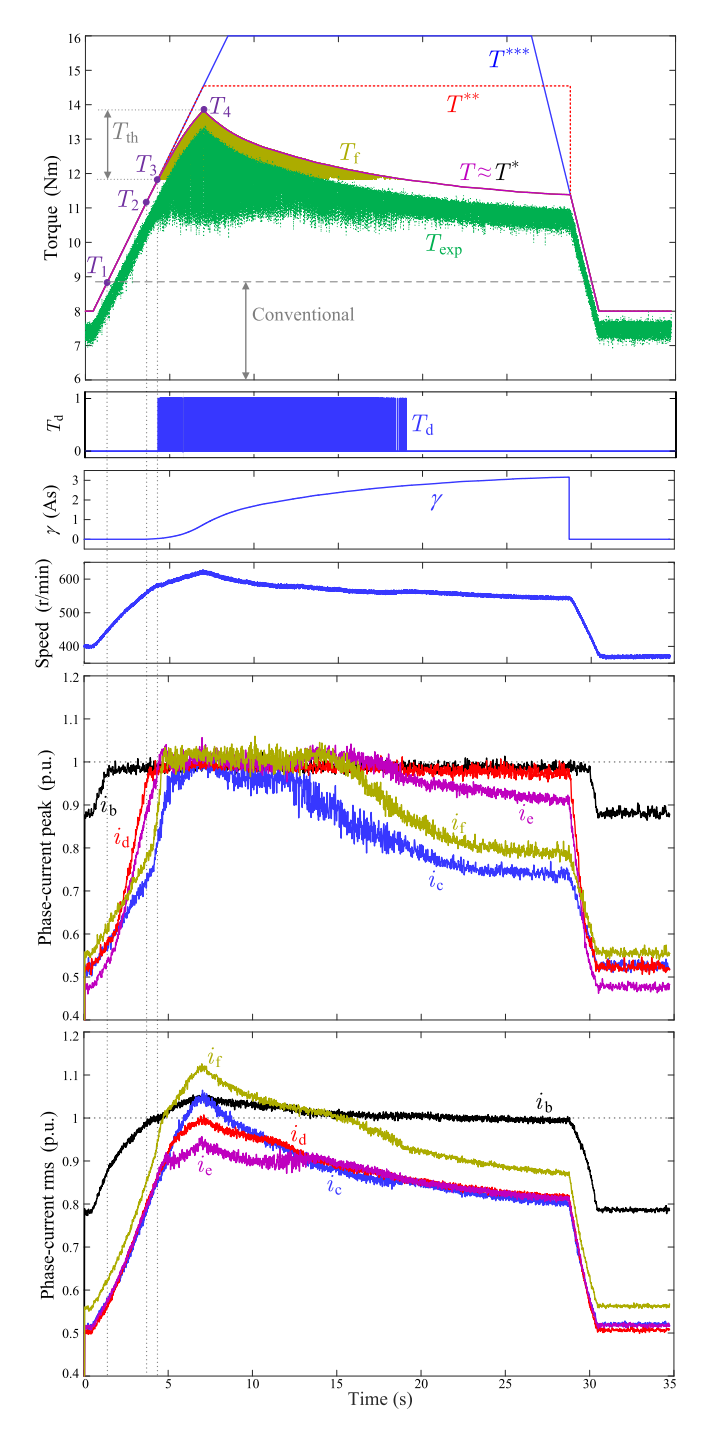


Fig. 18. Experimental transient results for consecutive gradual increase and reduction of the torque reference T^{***} , with phase a open.

reference torque and current signals instead of the measured ones, for a more accurate and general assessment, without the influence of measurement noise and control tracking error. In any case, although this article is focused on the current-reference generation and not on the current/torque control, it may be noted that the resulting currents track their references reasonably well, as shown in Fig. 19. This is so despite the speed variation. The current ripple that can be observed in Fig. 19 is due to the converter switching. The average switching frequency for Fig. 19(a)–(d) is 11.4, 11.5, 11.3, and 10.7 kHz, respectively, i.e., around 11 kHz in all cases. The

experimental torque $T_{\rm exp}$, also included in Figs. 18 and 19, follows $T_{\rm f}$ to a good extent as well. A certain (small) steady-state error is present due to the limitation of finite-control-set model predictive control in this regard [10], [46]; it could be corrected by an outer closed-loop speed/torque (e.g., proportional-integral) control [47] or by a disturbance estimator [48] if desired in a practical application (out of the scope of this article). Based on these results, the most important aspects of the behavior of the proposed NSBE-FRML reference-generation method are discussed next.

When the torque reference starts to rise in Fig. 18, all the currents increase linearly with it, and none of the peaks reach $i_{\rm pk}^{\rm mx}$ (1 p.u.), up to $T=T_1$. At T_1 , one of the phase currents (phase b) reaches 1 p.u., as shown in Fig. 19(a). Thus, for $T \leq T_1$, the proposed method is equivalent to the conventional MTPR one from [23] (or similar ones), described in Section II. The latter cannot achieve $T > T_1$, unless some phase-current peaks surpass 1 p.u. (in this case, overcurrent in phase b), or certain T_f ripple is allowed [23]. In contrast, the proposal yields greater T than T_1 without excessive peak current in any phase or $T_{\rm f}$ pulsation because of its ability to keep certain phase currents at 1 p.u., while the other ones adaptively ensure ripple-free T_f . This behavior can be seen in Fig. 19(b) and (c), and also seen in Fig. 18, for torque references up to T_3 . Regarding the rms current, to obtain higher torque values than T_2 , the rms needs to be temporarily raised over 1 p.u. in some phases, while respecting the maximum peak current, as shown in Fig. 18 and Table VII. Over T_2 , the algorithm for rms limitation (from Fig. 14) starts to reduce T^* below T^{**} slowly in Fig. 18, as γ accumulates the rms excess. Above T_3 , the torque reference T cannot be attained ($T_d = 1$) in the entire fundamental cycle, and certain ripple arises in $T_{\rm f}$. Although T^{***} keeps rising, T is effectively limited at $T_4 = T_3 + T_{th}$ by the proposal, so that the $T_{\rm f}$ pulsation never surpasses $T_{\rm th}$. Accordingly, the oscillations in T_{exp} are also restricted to a similar extent. When this happens, T^{**} is held by the algorithm from Fig. 15, while T continues being reduced exponentially by γ toward T_2 to limit the highest phase-current rms to 1 p.u. in steady state. Finally, as soon as T^{***} decreases and reaches T, γ is reset, and all torque-reference signals match again. In summary, the admissible torque has been extended by the proposal from T_1 to T_2 (steady state) or T_3 (transient overload) without T_f ripple, and to even higher torque values (such as T_4) with limited torque pulsation.

2) SCL Versus Torque: It should be remarked that, unlike MTPP strategies [17], [18], [19], [20], where the current is equally (highly) distorted for any load, the proposed NSBE-FRML reduces the current distortion, as the torque decreases from its maximum (see Fig. 19) so as to minimize the SCL per torque, in FRML manner. This FRML behavior is verified by comparing the SCL versus torque T of various approaches in Fig. 20, which is analogous to the theoretical ones from Figs. 2 and 14. Since the existing MTPP methods [17], [18], [19], [20] are not suitable for six-phase machines under an OPF because of their lack of generality, the MTPP current references in Fig. 20 are obtained by rescaling with T those of the proposal for the highest ripple-free torque T_3 , similar to the existing MTPP ones. Most importantly, in this figure,

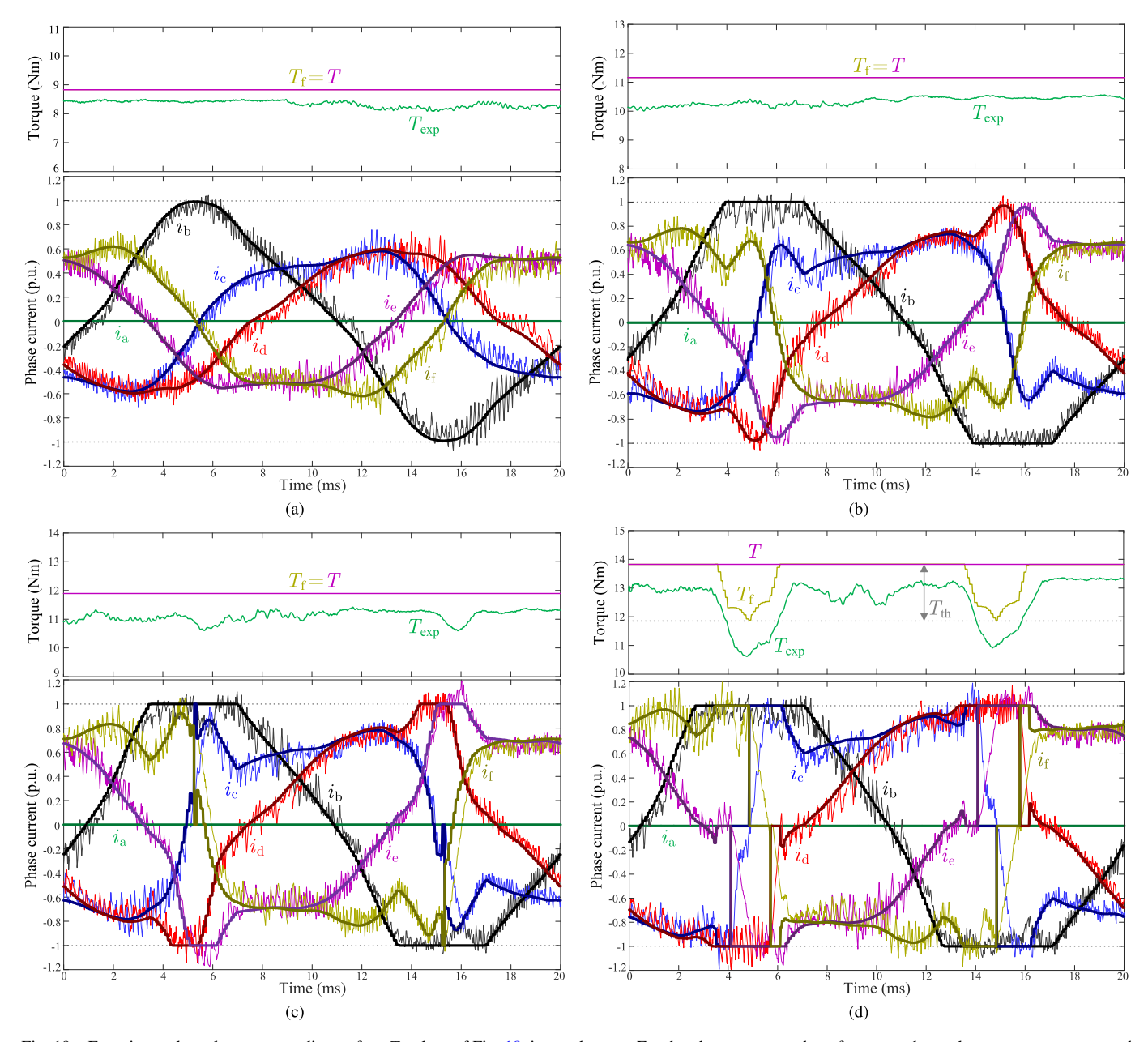


Fig. 19. Experimental results corresponding to four T values of Fig. 18, in steady state. For the phase currents, the reference and actual currents are represented by thick dark and thin bright lines, respectively. (a) Maximum T without reaching $i_{\rm pk}^{\rm mx}$ in any phase (maximum of conventional method), $T_1=0.53$ p.u. (b) Maximum T without exceeding $i_{\rm rms}^{\rm mx}$ in any phase, $T_2=0.67$ p.u. (c) Maximum T without $T_{\rm f}$ ripple during overload, $T_3=0.71$ p.u. (d) Maximum T with $T_{\rm f}$ ripple below $T_{\rm th}$ during overload, $T_4=0.83$ p.u.

TABLE VII EXPERIMENTAL PERFORMANCE OF THE PROPOSED METHOD IN STEADY STATE AT T_1 – T_4 FOR Phase a Open (Corresponding to Fig. 19)

T. (N.)	(T) ()	D 1.2	Torque ri-	Peak cu-	P	hase-cu	rrent r	ms (p.ı	1.)	nor ()
T (Nm)	T (p.u.)	Description	pple (Nm)	rrent (p.u.)	b	c	d	e	f	SCL (p.u.)
$\overline{}$ $< T_1$	<	$ i_k < i_{ m pk}^{ m mx}$ for any k (conventional)	0	<	<	<	<	<	<	<
$T_1 = 8.8$	0.53	Max. T without reaching $i_{\rm pk}^{\rm mx}$ for any k (conventional)	0	≈ 1	0.87	0.57	0.56	0.58	0.63	0.36
$T_2 = 11.2$	0.67	Max. T without exceeding $i_{\text{rms}}^{\text{mx}}$ for any k	0	≈ 1	1.00	0.78	0.79	0.80	0.85	0.60
$T_3 = 11.8$	0.71	Max. T without ripple in $T_{\rm f}$	0	≈ 1	1.01	0.86	0.86	0.88	0.94	0.69
$T_4 = 13.8$	0.83	Max. T with $T_{\rm f}$ ripple under $T_{\rm th}$	2	≈ 1	1.05	1.06	1.00	0.99	1.13	0.91

the SCL of the proposed NSBE-FRML is indeed minimized for each load value, being lower than the SCL of the MTPP method and matching the conventional MTPR [23] for $T \leq T_1$, providing the intended FRML characteristic. In other words,

both maximum torque range and minimum SCL per torque are accomplished.

It is also worth highlighting that, when the maximum torque is achieved during overload (T_3 or greater), the peak currents

TABLE VIII
EXECUTION TIME (μ s) OF CURRENT-REFERENCE GENERATION IN STEADY STATE AT T_1-T_4 FOR PHASE a OPEN (CORRESPONDING TO FIG. 19)

Method	Conventional								Prop	osed							
T	$\overline{T_1}$		7	Γ_1			7	I_2			2	Γ_3			2	Γ_4	
Block	Total	i gen.	$T_{ m th}$ lim.	rms lim.	Total	i gen.	$T_{ m th}$ lim.	rms lim.	Total	i gen.	$T_{ m th}$ lim.	rms lim.	Total	i gen.	$T_{ m th}$ lim.	rms lim.	Total
Max.	3.1	3.6	0.2	1.2	5.0	4.6	0.2	1.2	6.0	6.4	0.2	1.2	7.8	6.7	0.2	1.2	8.1
Avg.	2.9	3.4	0.2	0.3	3.9	3.7	0.2	0.3	4.2	3.9	0.2	0.3	4.4	4.4	0.2	0.3	4.9
Min.	2.7	3.2	0.2	0.3	3.7	3.2	0.2	0.3	3.7	3.2	0.2	0.3	3.7	3.2	0.1	0.3	3.6

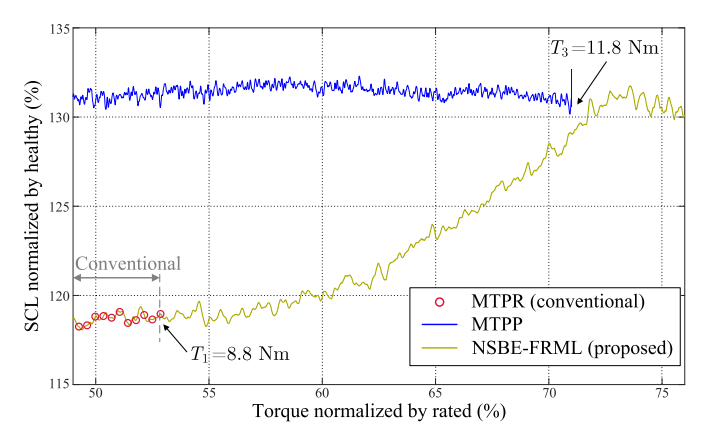


Fig. 20. Experimental SCL versus torque T for the conventional MTPR method [23], the proposed NSBE-FRML scheme, and MTPP method obtained by rescaling the current waveforms of $T_3 = 11.8$ Nm.

of all (or all but one) healthy phases match i_{nk}^{mx} [see Figs. 18 and 19(c) and (d)]. At the maximum steady-state torque after overload (i.e., T_2), the largest rms of the phase currents equals $i_{\rm rms}^{\rm mx}$, but this does not necessarily occur in the other healthy phases [see Figs. 18 and 19(b)]. The latter suggests that, although the proposed NSBE-FRML ensures that the torque capability is fully exploited during overload and the SCL is minimized at all times, there might still be room for further increasing the achievable torque in steady state while complying with the rms-current limitation. Optimizing the instantaneous currents with any degree of distortion during an entire fundamental cycle while considering the rms limits as inequality constraints in FRML fashion is far from being straightforward. It may be addressed in subsequent work. In any case, the increase in ripple-free torque reference attained by the proposal with respect to the conventional method is significant, both during $(T_3 \gg T_1)$ and after $(T_2 \gg T_1)$ overload.

3) Dynamic Response to Sudden Torque Step: Fig. 21 shows the response of the proposed NSBE-FRML method when the torque reference T^{***} is increased from below T_1 to over T_4 suddenly instead of gradually as in Fig. 17. It may be observed in Fig. 21 that the phase-current references, as well as the resulting current and torque, rise immediately with T^{***} as soon as it changes. In particular, the phase-current waveform shapes change very fast between those corresponding to Fig. 19(a) and (d). Furthermore, T is effectively limited to T_4 in Fig. 21 by the torque-ripple limitation block within half a fundamental cycle ($\tau_1/2$), so that the torque oscillation remains within T_{th} .

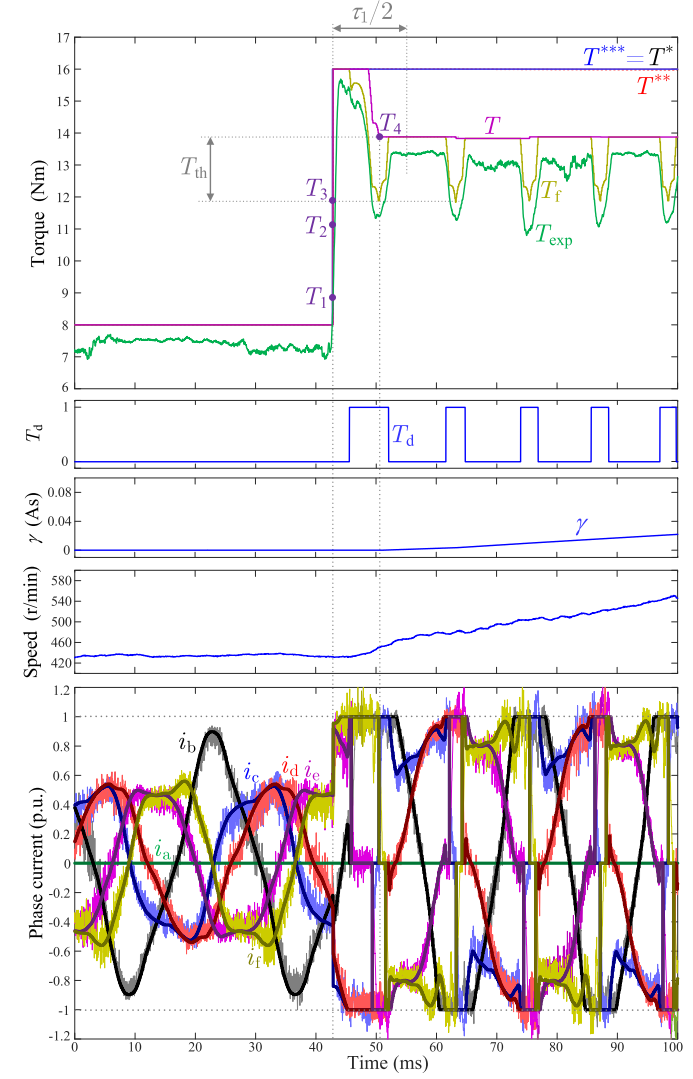


Fig. 21. Experimental transient results for sudden increase of the torque reference T^{***} , with phase a open.

C. Execution Time

Table VIII reflects the execution times in μ s of the conventional (see Section II) and proposed (i.e., NSBE-FRML) methods of current-reference generation obtained for T_1 - T_4 with phase a open at steady state (as in Fig. 19). For the proposal, the time is shown separately for each of the three blocks of the method that are depicted in Fig. 6, using the same colors. The time corresponding to the generation of the back EMF from the rotor position is also considered for both techniques, and for the NSBE-FRML, it is included as part of

TABLE IX
Values of T_1 – T_4 of the Torque Reference T for Various Scenarios of the Experimental Setup

/TI	D 11	Phases with OPFs													
<i>T</i>	Description	None	a	ab	ac	ad	af	abc	abd	ace	acf	abcd	abce	abde	abcf
T_1 (p.u.)	Max. T without reaching i_{pk}^{mx} for any k (conventional)	1.00	0.53	0.24	0.48	0.47	0.51	0.10	0.16	0.47	0.38	0.00	0.00	0.00	0.00
T_2 (p.u.)	Max. T without exceeding $i_{\text{rms}}^{\text{mx}}$ for any k	1.00	0.67	0.44	0.52	0.56	0.52	0.28	0.32	0.49	0.45	0.06	0.24	0.28	0.18
T_3 (p.u.)	Max. T without ripple in $T_{\rm f}$	1.08	0.71	0.28	0.55	0.54	0.56	0.10	0.16	0.47	0.38	0.00	0.00	0.00	0.00
T_4 (p.u.)	Max. T with T_{f} ripple under T_{th}							$T_3 +$	$T_{ m th}$						

the per-sample i generation (orange) block from Fig. 6. For each case in Table VIII, the maximum, average, and minimum execution times per fundamental cycle are given.

It can be seen in Table VIII that the total execution time of the proposal is moderately longer than for the conventional approach, and it tends to increase with T. Based on the times of each block, it may be concluded that this increase is mainly due to the per-sample i generation block, whose associated time is the greatest and is the only one that rises notably with T. The latter fact is because, as the torque reference rises, a greater number of phase currents need to be iteratively limited to $i_{\rm pk}^{\rm mx}$ in Fig. 7, which implies more iterations and, hence, increased operations. Nonetheless, the total required time is still acceptable, even in the most unfavorable conditions (8.1 μ s).

D. Torque Range for Other Scenarios

Table IX displays the values of T_1 - T_4 for other scenarios. Other possibilities of OPFs are equivalent to these ones because of symmetry [11]. For any of these situations, the proposal achieves larger torque than the conventional technique, which is limited to T_1 . In four cases of single or double OPFs, the maximum ripple-free torque is increased noticeably both during overload $(T_3 > T_1)$ and after it $(T_2 > T_1)$, as for phase a open. Without OPFs and overload, the attained ripplefree torque is not larger than with the conventional method $(T_2 \approx T_1 < T_3)$, but during overload, it is considerably increased $(T_3 > T_1)$. Something similar happens for phases a and f open. In eight cases that are particularly demanding (mostly of three or four OPFs), the highest ripple-free torque is not raised $(T_3 \approx T_1)$, but the average torque is made greater by allowing certain torque pulsation without rms excess $(T_2, T_4 > T_1, T_3)$. In conclusion, the proposed NSBE-FRML extends the torque range in all the scenarios, while respecting the drive limits and ensuring minimum SCL and torque ripple per average torque.

VIII. CONCLUSION

This article has proposed a general online method to generate current references for fault-tolerant multiphase PMSMs with negligible saliency ratio and with nonsinusoidal back EMF: the NSBE-FRML. Minimum SCL is attained when the torque reference is feasible, while maximizing the achievable value of the latter for given rated peak current, in FRML manner. For a higher torque reference, the instantaneous torque deviation is minimized. The torque reference is saturated

in consecutive samples to limit the torque pulsation if a prespecified ripple threshold is surpassed. Furthermore, the phase-current rms is limited to its rating after overload (e.g., during vehicle overtaking) by automatically decreasing the torque reference in a gradual fashion. The proposed NSBE-FRML can be applied to PMSMs of any power and phase number and with either symmetrical/asymmetrical windings, to both healthy and (any) OPF conditions, and to any back-EMF harmonics. The method is also suitable for PMSMs with sinusoidal back EMF, as a particular case. It is especially convenient for electric vehicles, where high torque capability and transient overload are crucial.

In summary, the main novelty of the new NSBE-FRML technique is that it ensures FRML; i.e., it combines the minimization of the SCL per torque and the maximization of the torque range. This kind of feature was available in the past for machines with sinusoidal back EMF, but not for nonsinusoidal back EMF, where special care needs to be paid to suitably shape the current waveforms with optimum harmonics. Moreover, this FRML property was also combined here with other desirable characteristics that were absent from most of the previous approaches: generality, lack of offline optimization, possible allowance of (limited) torque ripple for extended torque range, and automatic gradual transition from transient overload to steady state. These improvements are obtained at the expense of additional complexity and computational burden, but it is acceptable for modern digital signal processors.

The functionality of the proposed NSBE-FRML method has been verified by experimental tests with a six-phase PMSM with significant back-EMF harmonics (trapezoidal back EMF). For instance, compared with the conventional technique for minimum SCL, under an OPF, the maximum ripple-free torque was raised by 34% and 26% during and after overload, respectively; by allowing some (limited) torque pulsation, the torque increase was even greater.

Some subjects of future research are extending the NSBE-FRML to PMSMs with saliency, taking into account the effect of temperature or magnetic saturation on the back EMF, considering the torque ripple due to converter switching and cogging torque, incorporating a limitation to the voltage constraints for high speeds, or exploiting the maximum rms of all phases simultaneously in continuous operation.

REFERENCES

[1] M. J. Duran and F. Barrero, "Recent advances in the design, modeling, and control of multiphase machines—Part II," *IEEE Trans. Ind. Electron.*, vol. 63, no. 1, pp. 459–468, Jan. 2016.

- [2] A. G. Yepes, O. Lopez, I. Gonzalez-Prieto, M. J. Duran, and J. Doval-Gandoy, "A comprehensive survey on fault tolerance in multiphase AC drives, Part 1: General overview considering multiple fault types," *Machines*, vol. 10, no. 3, p. 208, Mar. 2022.
- [3] W. Taha, P. Azer, A. D. Callegaro, and A. Emadi, "Multiphase traction inverters: State-of-the-art review and future trends," *IEEE Access*, vol. 10, pp. 4580–4599, 2022.
- [4] M. Mengoni, L. Zarri, A. Tani, L. Parsa, G. Serra, and D. Casadei, "High-torque-density control of multiphase induction motor drives operating over a wide speed range," *IEEE Trans. Ind. Electron.*, vol. 62, no. 2, pp. 814–825, Feb. 2015.
- [5] Y. Hu, Z. Q. Zhu, and M. Odavic, "Torque capability enhancement of dual three-phase PMSM drive with fifth and seventh current harmonics injection," *IEEE Trans. Ind. Appl.*, vol. 53, no. 5, pp. 4526–4535, Sep. 2017.
- [6] A. Boglietti, I. R. Bojoi, S. Rubino, and M. Cossale, "Overload capability of multiphase machines under normal and open-phase fault conditions: A thermal analysis approach," *IEEE Trans. Ind. Appl.*, vol. 56, no. 3, pp. 2560–2569, May 2020.
- [7] I. Subotic, N. Bodo, E. Levi, and M. Jones, "Onboard integrated battery charger for EVs using an asymmetrical nine-phase machine," *IEEE Trans. Ind. Electron.*, vol. 62, no. 5, pp. 3285–3295, May 2015.
- [8] M. Y. Metwly, M. S. Abdel-Majeed, A. S. Abdel-Khalik, R. A. Hamdy, M. S. Hamad, and S. Ahmed, "A review of integrated on-board EV battery chargers: Advanced topologies, recent developments and optimal selection of FSCW slot/pole combination," *IEEE Access*, vol. 8, pp. 85216–85242, 2020.
- [9] Y. Sui, P. Zheng, Z. Yin, M. Wang, and C. Wang, "Open-circuit fault-tolerant control of five-phase PM machine based on reconfiguring maximum round magnetomotive force," *IEEE Trans. Ind. Electron.*, vol. 66, no. 1, pp. 48–59, Jan. 2019.
- [10] A. G. Yepes, I. Gonzalez-Prieto, O. Lopez, M. J. Duran, and J. Doval-Gandoy, "A comprehensive survey on fault tolerance in multiphase AC drives, Part 2: Phase and switch open-circuit faults," *Machines*, vol. 10, no. 3, p. 221, Mar. 2022.
- [11] W. N. W. A. Munim, M. J. Duran, H. S. Che, M. Bermodez, I. González-Prieto, and N. A. Rahim, "A unified analysis of the fault tolerance capability in six-phase induction motor drives," *IEEE Trans. Power Electron.*, vol. 32, no. 10, pp. 7824–7836, Oct. 2017.
- [12] H. S. Che, M. J. Duran, E. Levi, M. Jones, W. Hew, and N. A. Rahim, "Postfault operation of an asymmetrical six-phase induction machine with single and two isolated neutral points," *IEEE Trans. Power Electron.*, vol. 29, no. 10, pp. 5406–5416, Oct. 2014.
- [13] F. Baneira, J. Doval-Gandoy, A. G. Yepes, Ó. López, and D. Pérez-Estévez, "Control strategy for multiphase drives with minimum losses in the full torque operation range under single open-phase fault," *IEEE Trans. Power Electron.*, vol. 32, no. 8, pp. 6275–6285, Aug. 2017.
- [14] J. Sun, Z. Liu, Z. Zheng, and Y. Li, "An online global fault-tolerant control strategy for symmetrical multiphase machines with minimum losses in full torque production range," *IEEE Trans. Power Electron.*, vol. 35, no. 3, pp. 2819–2830, Mar. 2020.
- [15] G. Yang, H. Hussain, S. Li, J. Zhang, and J. Yang, "A unified fault-tolerant strategy for multiphase machine with minimum losses in full torque operation range based on closed-form expressions," *IEEE Trans. Power Electron.*, vol. 37, no. 10, pp. 12463–12473, Oct. 2022.
- [16] A. G. Yepes, A. Shawier, W. E. Abdel-Azim, A. S. Abdel-Khalik, S. Ahmed, and J. Doval-Gandoy, "General online current-harmonic generation for increased torque capability with minimum stator copper loss in fault-tolerant multiphase induction motor drives," *IEEE Trans. Transport. Electrific.*, early access, Feb. 13, 2023, doi: 10.1109/TTE.2023.3244742.
- [17] G. Feng, C. Lai, M. Kelly, and N. C. Kar, "Dual three-phase PMSM torque modeling and maximum torque per peak current control through optimized harmonic current injection," *IEEE Trans. Ind. Electron.*, vol. 66, no. 5, pp. 3356–3368, May 2019.
- [18] T. J. D. S. Moraes, H. Wu, E. Semail, N. K. Nguyen, and D. T. Vu, "Optimal torque/speed characteristics of a five-phase synchronous machine under peak or RMS current control strategies," in *Proc. 22nd Eur. Conf. Power Electron. Appl. (EPE ECCE Europe)*, Sep. 2020, pp. 1–7.
- [19] Z. Y. Gu, K. Wang, Z. Q. Zhu, Z. Z. Wu, C. Liu, and R. W. Cao, "Torque improvement in five-phase unequal tooth SPM machine by injecting third harmonic current," *IEEE Trans. Veh. Technol.*, vol. 67, no. 1, pp. 206–215, Jan. 2018.

- [20] K. Wang, Z. Q. Zhu, Y. Ren, and G. Ombach, "Torque improvement of dual three-phase permanent-magnet machine with third-harmonic current injection," *IEEE Trans. Ind. Electron.*, vol. 62, no. 11, pp. 6833–6844, Nov. 2015.
- [21] A. Cervone, O. Dordevic, and G. Brando, "General approach for modeling and control of multiphase PMSM drives," *IEEE Trans. Power Electron.*, vol. 36, no. 9, pp. 10490–10503, Sep. 2021.
- [22] A. Cervone, M. Slunjski, E. Levi, and G. Brando, "Optimal third-harmonic current injection for asymmetrical multiphase permanent magnet synchronous machines," *IEEE Trans. Ind. Electron.*, vol. 68, no. 4, pp. 2772–2783, Apr. 2021.
- [23] X. Kestelyn and E. Semail, "A vectorial approach for generation of optimal current references for multiphase permanent-magnet synchronous machines in real time," *IEEE Trans. Ind. Electron.*, vol. 58, no. 11, pp. 5057–5065, Nov. 2011.
- [24] A. Mohammadpour and L. Parsa, "Global fault-tolerant control technique for multiphase permanent-magnet machines," *IEEE Trans. Ind. Appl.*, vol. 51, no. 1, pp. 178–186, Jan. 2015.
- [25] M. Slunjski, O. Stiscia, M. Jones, and E. Levi, "General torque enhancement approach for a nine-phase surface PMSM with built-in fault tolerance," *IEEE Trans. Ind. Electron.*, vol. 68, no. 8, pp. 6412–6423, Aug. 2021.
- [26] G. Liu, Z. Lin, W. Zhao, Q. Chen, and G. Xu, "Third harmonic current injection in fault-tolerant five-phase permanent-magnet motor drive," *IEEE Trans. Power Electron.*, vol. 33, no. 8, pp. 6970–6979, Aug. 2018.
- [27] C. Xiong, T. Guan, P. Zhou, and H. Xu, "A fault-tolerant FOC strategy for five-phase SPMSM with minimum torque ripples in the full torque operation range under double-phase open-circuit fault," *IEEE Trans. Ind. Electron.*, vol. 67, no. 11, pp. 9059–9072, Nov. 2020.
- [28] D. T. Vu, N. K. Nguyen, E. Semail, and T. J. S. Moraes, "Control strategies for non-sinusoidal multiphase PMSM drives in faulty modes under constraints on copper losses and peak phase voltage," *IET Electric Power Appl.*, vol. 13, no. 11, pp. 1743–1752, Nov. 2019.
- [29] D. T. Vu, N. K. Nguyen, and E. Semail, "Fault-tolerant control for nonsinusoidal multiphase drives with minimum torque ripple," *IEEE Trans. Power Electron.*, vol. 37, no. 6, pp. 6290–6304, Jun. 2022.
- [30] N. Bianchi, S. Bolognani, and M. D. Pre, "Strategies for the fault-tolerant current control of a five-phase permanent-magnet motor," *IEEE Trans. Ind. Appl.*, vol. 43, no. 4, pp. 960–970, Aug. 2007.
- [31] M. Y. Metwly et al., "Investigation of six-phase surface permanent magnet machine with typical slot/pole combinations for integrated onboard chargers through methodical design optimization," *IEEE Trans. Transportort. Electrific.*, vol. 9, no. 1, pp. 866–885, Mar. 2023.
- [32] H. Zhang, H. Yin, W. Hua, X. Zhu, D. Gerada, and B. Wang, "The mechanism analysis on open-circuit back EMF in fractional-slot concentrated winding permanent magnet machines using air-gap field modulation theory," *IEEE Trans. Transport. Electrific.*, vol. 7, no. 4, pp. 2658–2670, Dec. 2021.
- [33] V. I. Patel, J. Wang, and S. S. Nair, "Demagnetization assessment of fractional-slot and distributed wound 6-phase permanent magnet machines," *IEEE Trans. Magn.*, vol. 51, no. 6, pp. 1–11, Jun. 2015.
- [34] Y. Fan, R. Cui, and A. Zhang, "Torque ripple minimization for interturn short-circuit fault based on open-winding five phase FTFSCW-IPM motor for electric vehicle application," *IEEE Trans. Veh. Technol.*, vol. 69, no. 1, pp. 282–292, Jan. 2020.
- [35] A. S. Abdel-Khalik, S. Ahmed, A. M. Massoud, and A. A. Elserougi, "An improved performance direct-drive permanent magnet wind generator using a novel single-layer winding layout," *IEEE Trans. Magn.*, vol. 49, no. 9, pp. 5124–5134, Sep. 2013.
- [36] A. M. El-Refaie, "Fractional-slot concentrated-windings synchronous permanent magnet machines: Opportunities and challenges," *IEEE Trans. Ind. Electron.*, vol. 57, no. 1, pp. 107–121, Jan. 2010.
- [37] F. Wu, C. Tong, Y. Sui, L. Cheng, and P. Zheng, "Influence of third harmonic back EMF on modeling and remediation of winding short circuit in a multiphase PM machine with FSCWs," *IEEE Trans. Ind. Electron.*, vol. 63, no. 10, pp. 6031–6041, Oct. 2016.
- [38] A. G. Yepes et al., "General open-phase fault-tolerant online current-reference generation for maximum torque range and minimum copper loss with phase-current-peak limitation for *n*-phase PMSMs with non-sinusoidal back-EMF," in *Proc. IEEE ECCE*, Oct. 2023, pp. 1–8.
- [39] T. Lazzari, F. Scalcon, C. Volpato, T. Gabbi, M. Stefanelo, and R. P. Vieira, "Sensorless control of nonsinusoidal back-EMF PMSM based on state observer," in *Proc. IEEE 15th Brazilian Power Elec*tron. Conf. 5th IEEE Southern Power Electron. Conf. (COBEP/SPEC), Dec. 2019, pp. 1–6.

- [40] L. R. Rocha and R. P. Vieira, "Design methodology and analysis of back-EMF observers for non-sinusoidal PMSM in electric vehicle traction," *J. Control, Autom. Electr. Syst.*, vol. 33, no. 1, pp. 315–325, Feb. 2022.
- [41] X. Wang, Z. Wang, Z. Xu, W. Wang, B. Wang, and Z. Zou, "Deadbeat predictive current control-based fault-tolerant scheme for dual threephase PMSM drives," *IEEE J. Emerg. Sel. Topics Power Electron.*, vol. 9, no. 2, pp. 1591–1604, Apr. 2021.
- [42] J. Qu, C. Zhang, J. Jatskevich, and S. Zhang, "Deadbeat harmonic current control of permanent magnet synchronous machine drives for torque ripple reduction," *IEEE J. Emerg. Sel. Topics Power Electron.*, vol. 10, no. 3, pp. 3357–3370, Jun. 2022.
- [43] A. G. Sarigiannidis, F. A. Karamountzou, and A. G. Kladas, "Model predictive torque control with low torque ripple for interior PM motor variable speed drives," in *Proc. 13th Int. Conf. Electr. Mach. (ICEM)*, Sep. 2018, p. 1604.
- [44] S. B. Ozturk and H. A. Toliyat, "Direct torque and indirect flux control of brushless DC motor," *IEEE/ASME Trans. Mechatronics*, vol. 16, no. 2, pp. 351–360, Apr. 2011.
- [45] A. Shawier et al., "Effect of winding design on the performance of predictive current control of six-phase induction machine-based propulsion systems," *IEEE Access*, vol. 10, pp. 80587–80599, 2022.
- [46] H. A. Young, M. A. Perez, J. Rodriguez, and H. Abu-Rub, "Assessing finite-control-set model predictive control: A comparison with a linear current controller in two-level voltage source inverters," *IEEE Ind. Electron. Mag.*, vol. 8, no. 1, pp. 44–52, Mar. 2014.
- [47] K. Li, T. Sun, F. Jiang, W. Feng, and H. Li, "MTPA control for IPMSM drives based on pseudorandom frequency-switching sinusoidal signal injection," *Machines*, vol. 10, no. 4, p. 231, Mar. 2022.
- [48] M. Bermudez, M. R. Arahal, M. J. Duran, and I. Gonzalez-Prieto, "Model predictive control of six-phase electric drives including ARX disturbance estimator," *IEEE Trans. Ind. Electron.*, vol. 68, no. 1, pp. 81–91, Jan. 2021.



Alejandro G. Yepes (Senior Member, IEEE) received the M.Sc. and Ph.D. degrees in electrical engineering from the Universidade de Vigo, Vigo, Spain, in 2009 and 2011, respectively.

From August 2016 to June 2018, he was a Visiting Scholar with the Department of Electrical and Computer Engineering, Texas A&M University, College Station, TX, USA, after which he returned to Universidade de Vigo. Since 2008, he has been working with the Applied Power Electronics Technology Research Group, Universidade de Vigo. His research

interests include the areas of ac power conversion, with a special focus, currently, on multiphase drives.



Wessam E. Abdel-Azim received the B.Sc. degree in electrical engineering from Alexandria University, Alexandria, Egypt, in 2018.

He is currently a Teaching Assistant with the Department of Electrical, Faculty of Engineering, Alexandria University. His current research interests include electric drives, power electronics, and pulsed power applications.



Abdullah Shawier received the B.Sc. and M.Sc. degrees in electrical engineering from Alexandria University, Alexandria, Egypt, in 2016 and 2021, respectively.

He is currently a Lecturer Assistant with the Electrical Engineering Department, Faculty of Engineering, Alexandria University. His current research interests include electric drives, multiphase machine, model predictive control, battery chargers, and power electronics.



Ayman Samy Abdel-Khalik (Senior Member, IEEE) received the B.Sc. and M.Sc. degrees in electrical engineering from Alexandria University, Alexandria, Egypt, in 2001 and 2004, respectively, and the Ph.D. degree in electrical engineering from Alexandria University, and Strathclyde University, Glasgow, U.K., under a dual-channel program, in 2009.

He is currently a Professor with the Electrical Engineering Department, Faculty of Engineering, Alexandria University. His current research interests

include electrical machine design and modeling, electric drives, energy conversion, and renewable energy.

Dr. Abdel-Khalik serves as the Editor-in-Chief for the *Alexandria Engineering Journal*. He also serves as an Associate Editor for the IEEE Transactions on Industrial Electronics and the *IET Electric Power Applications Journal*.



Mostafa S. Hamad (Senior Member, IEEE) received the B.Sc. and M.Sc. degrees in electrical engineering from Alexandria University, Alexandria, Egypt, in 1999 and 2003, respectively, and the Ph.D. degree in electrical engineering from Strathclyde University, Glasgow, U.K., in 2009.

He is currently a Professor with the Department of Electrical and Control Engineering, College of Engineering and Technology, Arab Academy for Science, Technology and Maritime Transport (AASTMT), Al Alamein, Egypt. His research interests include

power electronics applications in power quality, electric drives, distributed generation, HVDC transmission systems, and renewable energy.



Shehab Ahmed (Senior Member, IEEE) received the B.Sc. degree from Alexandria University, Alexandria, Egypt, in 1999, and the M.Sc. and Ph.D. degrees from Texas A&M University, College Station, TX, USA, in 2000 and 2007, respectively.

He was with Schlumberger Technology Corporation, Houston, TX, USA, from 2001 to 2007, developing downhole mechatronic systems for oilfield service products. He was with Texas A&M University at Qatar, Ar-Rayyan, Qatar, from 2007 to 2018. He is currently a Professor and the Chair of the Elec-

trical and Computer Engineering Program, CEMSE Division, King Abdullah University of Science and Technology, Thuwal, Saudi Arabia. His research interests include subsurface mechatronics, solid-state power conversion, electric machines, and drives.



Jesús Doval-Gandoy (Member, IEEE) received the M.Sc. degree in electrical engineering from the Polytechnic University of Madrid, Madrid, Spain, in 1991, and the Ph.D. degree from the Universidade de Vigo, Vigo, Spain, in 1999.

He is currently a Professor and the Head of the Applied Power Electronics Technology Research Group (APET), Universidade de Vigo. His research interests include the areas of ac power conversion.